Acta Materialia 281 (2024) 120388

Contents lists available at ScienceDirect

Acta Materialia

journal homepage: www.elsevier.com/locate/actamat

Improvement of magnetic properties and hardness by alloying Mo to a FeCrCo alloy

Zhaolong Xiang [a,b,c], Engang Wang [d], Tao Wang [a], Bailing An [b,e], Yan Xin [b], Jun Lu [b], Rongmei Niu [b], Zhishan Mi [f], Wenqing Wei [c], Baode Sun [a], Ke Han [b,*], Xi Li [a,*]

[a] State Key Laboratory of Clean and Efficient Turbomachinery Power Equipment, Shanghai Jiao Tong University, Shanghai 200240, China
[b] National High Magnetic Field Laboratory, Florida State University, Tallahassee, FL 32310, United States
[c] School of Machinery and Automation, Weifang University, Weifang 261061, China
[d] Key Laboratory of Electromagnetic Processing of Materials (Ministry of Education), Northeastern University, Shenyang 110819, China
[e] State Key Laboratory of Materials Processing and Die & Mould Technology, Huazhong University of Science and Technology, Wuhan 430074, China
[f] Material Digital R&D Center, China Iron & Steel Research Institute Group, Beijing 100081, China

ARTICLE INFO

Keywords:
FeCrCoMo alloy
Magnetic properties
Spinodal decomposition
First-principles calculations

ABSTRACT

In most of the technologies used for improving material properties, the enhancement of some properties usually leads to the degradation of others. In this study, we demonstrated that we were able to simultaneously improve hardness, coercivity, and remanence by alloying an FeCrCo alloy with Mo by engineering its $\alpha \rightarrow \alpha_1 + \alpha_2$ spinodal decomposition. We prepared six Mo-alloyed samples and subjected them to the appropriate aging protocols. As aging progressed, hardness increased from 272 to 447 HV and coercivity increased from 47 to 592 Oe in the alloyed samples. Remanence gradually increased from 52 to 98 Am^2/kg, and then decreased to 82 Am^2/kg in the final stage of the aging process. By adding Mo to six individual FeCrCo samples aged to different stages, we increased the hardness of these samples by 3 %, 8 %, 7 %, 8 %, 5 %, and 10 %, respectively. At the same time, we increased their coercivity by 74 %, 13 %, 19 %, 4 %, 14 %, and 9 % respectively and their remanence by 82 %, 63 %, 4 %, 4 %, 9 %, and 13 %, respectively. We used data drawn from scanning transmission electron microscopy, first-principles calculations, and magnetic force microscopy in order to elucidate the reasons behind the observed enhancements of magnetic properties in the FeCrCoMo alloy.

1. Introduction

Because of the wide-ranging applications of magnetic materials in electric vehicles, sensors, magnetic bearings, wind turbines, and the like, such materials have attracted considerable attention from researchers [1-5]. Two of these materials, NdFeB [6-9] and SmCo [10-13], which contain rare-earth metals, are renowned for their exceptional magnetic properties. Like other magnetic materials containing rare-earth elements, however, these two have certain disadvantages. They often exhibit poor mechanical properties, and the extraction of the necessary rare earth metals is costly and time-consuming. Other permanent magnet alloys like AlNiCo and FeCrCo, which are free of rare-earth metals, are often used as substitutes. Of these two, FeCrCo, which was initially developed in the 1970s [14-16], is far superior in machinability compared not only with rare earth magnetic materials but also with AlNiCo [17-19].

FeCrCo alloys exhibit a miscibility gap at approximately 700 °C [20-23]. When these alloys are aged within this range, spinodal decomposition occurs, i.e., the supersaturated mother body-centered cubic (BCC) α phase decomposes into daughter BCC-α_1 and BCC-α_2 phases. The compositions of the α_1 and α_2 daughter phases are different from that of the α mother phase [24,25]. The α_1 phase, which is enriched in Fe and Co, exhibits ferromagnetic properties, whereas the α_2 phase, which is enriched in Cr, displays weak magnetic characteristics. This indicates that the magnetic properties of FeCrCo alloys are primarily determined by the size, volume, and composition of the α_1 phase, as well as by the lattice mismatch between the α_1 and α_2 phases. Consequently, the primary approach to improving magnetic properties is through optimizing these parameters.

Several research groups have optimized the magnetic properties of FeCrCo alloys by implementing various step-aging heat treatments [26-29]. As yet, however, no researchers have analyzed such results at

* Corresponding authors.
E-mail addresses: han@magnet.fsu.edu (K. Han), lx_net@sina.com (X. Li).

https://doi.org/10.1016/j.actamat.2024.120388
Received 14 December 2023; Received in revised form 28 August 2024; Accepted 8 September 2024
Available online 12 September 2024

sub-micron scale or atomic scale. We decided to do so by investigating the question of why such excellent magnetic properties can result from spinodal decomposition in FeCrCo alloys. We are now focused on studying how these magnetic properties are affected by changes in the volume, lattice mismatch, and/or composition of α_1 and α_2 phases. To enhance magnetic properties, certain research groups have introduced high magnetic fields during heat treatment, causing the α_1 phase to elongate and line up parallel to the direction of the magnetic field [30-34]. Several studies have shown that the magnetic properties of FeCrCo can be enhanced by adding Mo [35-39]. Many researchers have successfully improved magnetic properties using the above-mentioned methods, but several scientific problems persist. The relationship remains largely unclear between atomic scale microstructure and magnetic properties in FeCrCoMo alloys. Certain questions remain: 1) what is the effect on magnetic properties brought about by the evolution of the magnetic domain of the alloys during the process of spinodal decomposition; 2) what is the effect on spinodal microstructure brought about by adding Mo, especially with respect to the composition, the volume, and the size of the hard α_1 phase; 3) what is the effect of Mo addition on the compositional gap and the lattice strain between the hard α_1 and soft α_2 phases; and 4) how can we best describe the evolution of the magnetic moments of spinodal phases during the process of spinodal decomposition.

To address these problems, we fabricated a series of hard magnetic 56.4Fe29Cr14Co0.6Mo samples by using various step-aging processes. Using High-Angle Annular Dark Field-Scanning Transmission Electron Microscopy (HAADF-STEM), we subsequently analyzed the size, volume, lattice mismatch, and composition of the α_1 and α_2 phases in each sample. Afterward, using the crystallographic and compositional data of the spinodal phases, obtained from X-ray Diffraction (XRD) and STEM-Energy Dispersive Spectroscopy (STEM-EDS), we calculated the electronic Density Of States (DOS) and the magnetic moment of each phase, using first-principles calculations based on Density Functional Theory (DFT). In addition, using Atomic Force Microscopy (AFM), we observed the evolution of the magnetic domain while spinodal decomposition was in progress. Combining experimental and calculated results, we systematically explored the effect of Mo addition on the spinodal structures of the 56.4Fe29Cr14Co0.6Mo samples. In this way, we revealed the impact of structure on either the magnetic properties or the hardness of our samples. Our investigations have opened new possibilities for designing and optimizing hard magnetic materials in the future.

2. Experimental procedures

2.1. Sample preparation

By applying vacuum arc melting in a high-purity Ar atmosphere, we fabricated one Mo- alloyed ingot with nominal composition of 56.4Fe29Cr14Co0.6Mo (atomic percent, at.%). The purity of the raw materials was higher than 99.95 wt.%. The ingot was re-melted at least five times and flipped each time to enhance chemical homogeneity. Afterward, the as-cast ingot was solution-treated (ST) at 1300 °C for 4 h in an Ar atmosphere with the aim of forming a completely homogeneous solid solution. The ST ingot was then subjected to water quenching. Subsequently, from the center of the ST ingot, we cut seven samples (ST and AT1–6), each measuring $15 \times 10 \times 5$ mm^3. Sample ST received only solution treatment. To investigate the influence of Mo on microstructural evolution and magnetic properties as aging time progressed, the remaining six samples underwent various aging treatments (AT). Specifically, samples AT1-AT6 were aged at 645 °C for 1 hour; samples AT2-AT6 received additional aging at 620 °C for 1 hour; samples AT3-AT6 received additional aging at 600 °C for 2 h; samples AT4-AT6 received additional aging at 580 °C for 3 h; samples AT5 and AT6 received additional aging at 560 °C for 4 h; sample AT6 received additional aging at 540 °C for 5 h, followed by further aging at 520 °C for 6 h (Table 1). All the aged samples were air-cooled to room temperature.

Table 1
Heat treatment of each aging treated sample.

Sample	Heat treatment
AT1	645 °C, 1 h
AT2	645 °C, 1 *h* + 620 °C, 1 h
AT3	645 °C, 1 *h* + 620 °C, 1 *h* + 600 °C, 2 h
AT4	645 °C, 1 *h* + 620 °C, 1 *h* + 600 °C, 2 *h* + 580 °C, 3 h
AT5	645 °C, 1 *h* + 620 °C, 1 *h* + 600 °C, 2 *h* + 580 °C, 3 h, + 560 °C, 4 h
AT6	645 °C, 1 *h* + 620 °C, 1 *h* + 600 °C, 2 *h* + 580 °C, 3 h, + 560 °C, 4 *h* + 540 °C, 5 h,+520 °C, 6 h

2.2. Microstructural analysis

All solution-treated and aging-treated samples were first polished, then subjected to examination in a D8 Advance DaVinci X-ray diffractometer (Bruker, Germany) in order to determine phase presence. To examine the evolution of composition and microstructure during spinodal decomposition, we sliced a thin specimen sheet ($10 \times 10 \times 0.5$ mm^3) from the center of each aging-treated sample. To prepare the STEM specimens, we ground each of the six sheets into a foil, 50 μm thick. Two disks with a diameter of 3 mm were punched out from each foil, then ground to a thickness of approximately 30 μm, and subsequently subjected to argon ion-beam milling at 5 keV and 7°, using a precision ion polishing system (PIPS 691, Gatan Inc., USA). The microstructure and composition of these discs were observed in a JEM-ARM200CF scanning transmission electron microscope (JEOL, Japan) equipped with an EDS system. An open-source software Strain++ for Geometric Phase Analysis (GPA) was used to analyze the coherent strain field from atomic-resolution HAADF-STEM images [40]. Magnetic Force Microscopy (MFM) with an MFP-3D AFM (Asylum Research, USA) was used to analyze the magnetic domain structure of our samples.

2.3. First-principles calculations

To thoroughly understand the effect of Mo alloying on the relationship between microstructure and magnetic properties in the 56.4Fe29Cr14Co0.6Mo alloy, we calculated the magnetic moments and electronic DOS of the spinodal phases using first-principles calculations based on the DFT within the Vienna Ab-initio Simulation Package (VASP) [41,42]. We built atomic structure models using both the crystallographic structure and the chemical composition obtained from the XRD and STEM-EDS analyses. The first-principles calculations were performed using a plane-wave code with Projector Augmented Wave (PAW) potentials and an exchange correlation function with the Perdew Burke Ernzerhof (PBE) Generalized Gradient Approximation (GGA). The Monkhorst−Pack k-point grids were set to $5 \times 5 \times 5$ for the calculation of the α_1 and α_2 supercells (α_1, α_2 = 128 atoms) [43]. The plane wave cutoff energy was set to 500 eV and the forces on all the atoms were $<$0.01 eV/Å during the geometrical optimization. For the magnetic moment calculations, the total energy convergence was 5−10 eV and the spin-polarization parameter was set to 2. Random atomic arrangements of the α_1 and α_2 phases were constructed using Special Quasi-random Structures (SQS) and the Alloy Theoretic Automated Toolkit (ATAT) software package (Fig. S1).

2.4. Testing of properties and magnetostriction coefficient

At 298 K, the hysteresis loop of each aging-treated sample was examined using a Vibrating Sample Magnetometer (VSM) that was installed within a Physical Property Measurement System (PPMS). From each sample, we prepared a specimen with a diameter of 3 mm and a thickness of 20 μm to eliminate the influence of the demagnetizing factor on magnetic property testing (Fig. S2). We polished the largest surface of each aging-treated sample and tested the Vickers hardness in the vicinity of the surface center using a diamond indenter under a load of 0.5 kg for a dwelling time of 10 s with a Tukon 2100 microhardness

tester (Wilson/Instron, USA). The magnetostriction coefficient of the 56.4Fe29Cr14Co0.6Mo alloy was determined using a BKT-2600 electric hysteresis loop tester (Beijing New Science High-Tech Technology Co., Ltd., China).

3. Results

3.1. Crystal structure evolution based on XRD and STEM

Using XRD, we characterized the phase constitution of 56.4Fe29Cr14Co0.6Mo alloy after spinodal decomposition. In sample ST, we found only the α phase, which had a BCC crystal structure (Fig. 1). In samples AT1–AT6, we expected that the α phase would have decomposed into the BCC-α_1 and BCC-α_2 phases, but with our current XRD technology, we were not able to see distinctly separated peaks from those two phases. This observation is similar to that reported in previous XRD studies on FeCrCo [44]. When we analyzed the Full Width at Half Maximum (FWHM) for the α_1 and α_2 phases from the (110), (200), and (211) reflections for aged samples, we found that the average FWHM values of both α_1 and α_2 phases increased steadily as spinodal decomposition progressed (Table 2). These increases were accompanied by a gradual separation of the XRD peaks of the α_1 phase from those of the α_2 phase, even though these peaks remained overlapped to some degree. We also calculated the average lattice parameters of the α_1 and α_2 phases from the (110), (200), and (211) reflections for aged samples. Based on the lattice parameters of the two phases, we calculated the lattice misfit between them for samples AT1–AT6. Our results indicated that lattice misfit values increased steadily as spinodal decomposition progressed (Table 2).

We analyzed the morphology and composition of the modulated structure at the nanometer and atomic scales by subjecting all aged samples to STEM. In each of the samples that underwent aging treatment, we could clearly observe a typical morphology of the modulated structure, i.e., many bright α_1 particles were dispersed throughout the adjacent dark α_2 matrix (Figs. 2a–f). Our Fast Fourier Transform (FFT) analyses indicated that both phases exhibited a BCC structure. Using STEM-HAADF images of samples AT1–AT6, we explored the evolution of volume percentage and diameter of the α_1 phase during the spinodal decomposition process. Our results showed that the average diameter of the α_1 phase was gradually increased from samples AT1 to AT6 (Fig. 2h). We observed an increase in the volume percentage of the α_1 phase from samples AT1 to AT3, followed by stabilization from samples AT3 to AT6 (Fig. 2g). We compared these results with those of our previous study [45]. We found that alloying with 0.6 at% Mo changed the average diameter of the α_1 phase, increasing it by 68 %, 1 %, 0.4 %, 15 %, and 9 % for samples AT1–AT5, respectively, and decreasing it by 10 % for sample AT6. The volume percentage of the α_1 phase increased by 22 %, 2 %, 7 %, 7 %, 8 %, and 7 % for samples AT1–AT6, respectively. This evolution in the volume percentage and diameter of the α_1 phase reflects the changes in the magnetic properties, which will be discussed in Section 4.2.

Table 2
The average values of FWHM, lattice parameters of the α_1 and α_2 phases, and the lattice misfit between the two phases for aging-treated samples (AT1-AT6). The lattice parameter values are calculated using the Bragg reflection angles (2θ) of (110), (200), and (211). The data processing procedure is shown in supplementary material (Fig. S3).

Sample	FWHM		Lattice parameter		Lattice misfit
	α_1 phase	α_2 phase	α_1 phase	α_2 phase	
AT1	0.4919 ± 0.1442	0.4658 ± 0.1996	0.2876 ± 0.0002	0.2879 ± 0.0003	0.0012± 0.0003
AT2	0.4811 ± 0.1670	0.5166 ± 0.2048	0.2875 ± 0.0002	0.2881 ± 0.0003	0.0020± 0.0003
AT3	0.5224 ± 0.1526	0.5601 ± 0.1698	0.2874 ± 0.0003	0.2881 ± 0.0003	0.0024± 0.0003
AT4	0.5488 ± 0.1586	0.6090 ± 0.2008	0.2872 ± 0.0004	0.2882 ± 0.0003	0.0034± 0.0003
AT5	0.5670 ± 0.1641	0.6233 ± 0.2045	0.2872 ± 0.0003	0.2883 ± 0.0002	0.0039± 0.0003
AT6	0.6783 ± 0.0734	0.6798 ± 0.2295	0.2871 ± 0.0003	0.2884 ± 0.0003	0.0047± 0.0003

To investigate the element distribution in the α_1 and α_2 phases during spinodal decomposition, STEM-EDS maps were made in samples AT1-AT6, showing a predominance of Co and Fe in the bright α_1 and Cr in the dark α_2 (Fig. 3). The concentration of Mo, however, was unclear. Our calculations of local average composition in the two phases for samples AT1–AT6, however, indicated that Mo was enriched in the α_2 phase (Fig. 4). In the α_1 phase, the intensity of composition fluctuation consistently increased in Fe and Co and consistently decreased in Cr from samples AT1–AT6 (Fig. 4a). However, in the α_2 phase, the fluctuation trends of the three elements were opposite to those in the α_1 phase, i.e., the fluctuation intensity of Co and Fe consistently decreased,

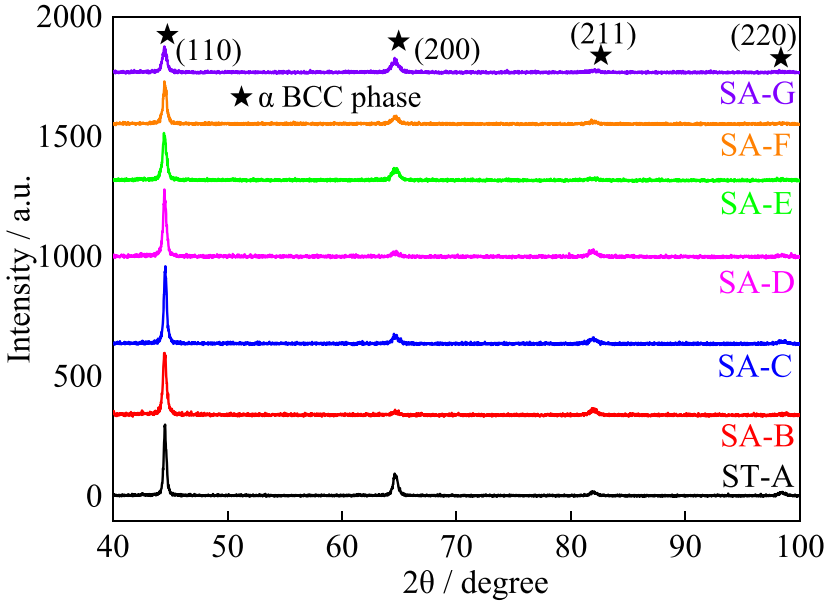

Fig. 1. XRD patterns of the solution-treated (ST) and aging-treated (AT1-AT6) samples. All samples exhibited the BCC structure.

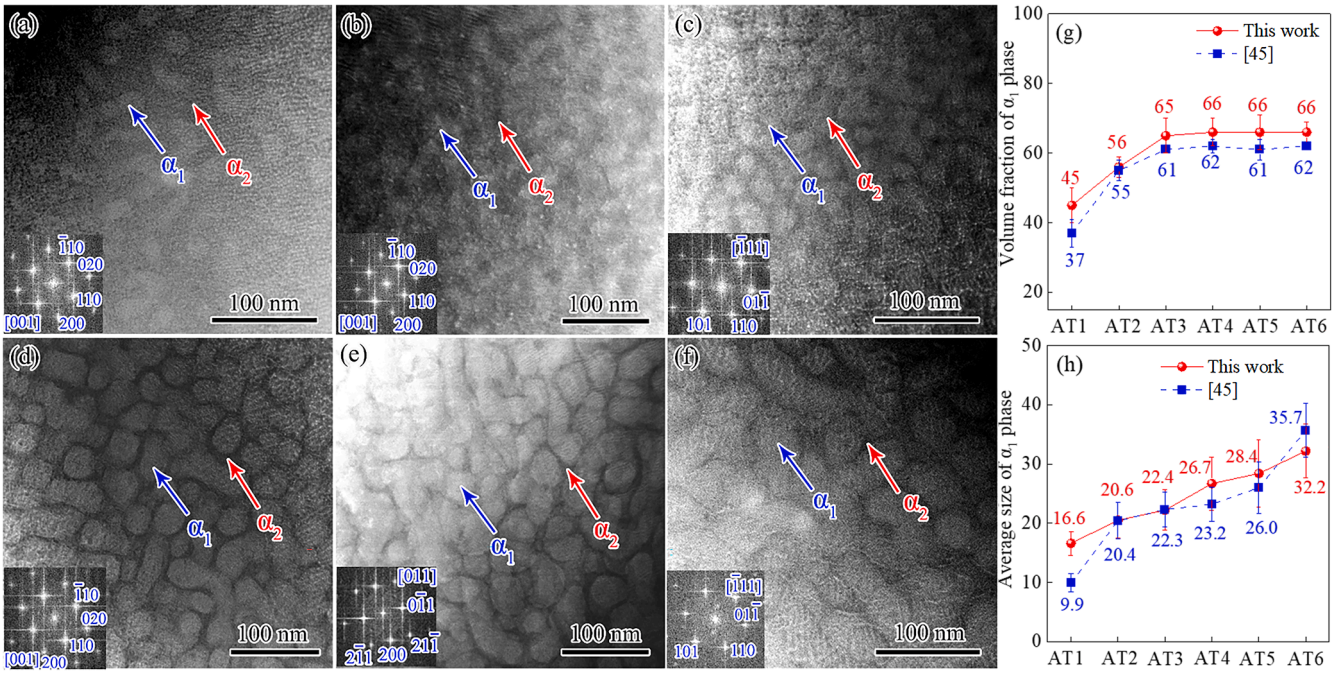

Fig. 2. HAADF-STEM images and analyses of volume percentage and average diameter of the α_1 phase in each sample after aging treatment. (a) AT1, (b) AT2, (c) AT3, (d) AT4, (e) AT5, and (f) AT6. FFT data in the insets show that the zone axis of samples AT1, AT2, and AT4 is [001], that of sample AT5 is [011], and that of samples AT3 and AT6 is [111]. Each inserted FFT image is derived from the corresponding atomic-resolution HAADF image shown in Fig. 5. (g) Volume percentage and (h) average diameter of the α_1 phase. (Fig. 2g and Fig. 2h include the volume percentage and average diameter of the α_1 phase of each non-alloyed sample [45]).

while that of Cr consistently increased (Fig. 4b). Upon comparison of these values with our previous results [45], we found that the intensity of the composition fluctuation in each of the samples alloyed with Mo was higher than that of the corresponding non-alloyed samples, indicating an increase in magnetic properties after alloying with Mo.

We further conducted a detailed investigation of the lattice parameters for the α_1 and α_2 phases in samples AT1–AT6. Using atomic-resolution HAADF-STEM images, we measured the lattice spacing in two directions in both phases for each aging-treated sample (Figs. 5a–f). We then calculated average lattice parameters for the two phases (Fig. 6a). In our previous studies involving Mo-free samples, the lattice parameter of the α_1 phase was found to be greater than that of the α_2 phase [46]. In Mo-alloyed samples, by contrast, the lattice parameter of the α_1 phase was found to be smaller than that of the α_2 phase. STEM-EDS data showed that Mo was enriched in the α_2 phase and poor in the α_1 phase (Fig. 4), indicating that additional lattice distortion was introduced in the α_2 phase because the atomic radius of Mo is larger than that of either Fe, Cr or Co. This may be the main reason why, in all Mo-alloyed samples, the lattice parameter is larger in the α_2 phase than in the α_1 phase.

Using first-principles calculations based on 128-atom supercells (Fig. S1), we also calculated the lattice parameters of the α_1 and α_2 phases for samples AT1–AT6 (Fig. 6a). These values indicated that the lattice parameter of the α_1 phase consistently increased from samples AT1 to AT6. For the α_2 phase, however, the lattice parameter consistently decreased from samples AT1 to AT6. These variations in the lattice parameter reflect the evolution of the composition during the process of spinodal decomposition. Using the lattice parameter values of the two phases (as determined from both HAADF images and first-principles calculations), we then calculated the lattice mismatch between them for samples AT1–AT6. Both these calculation methods indicated that the lattice mismatch gradually increased from samples AT1 to AT6 (Fig. 6b).

3.2. Magnetic properties

We measured the hysteresis loops of samples AT1–AT6, which were heated at various temperatures for various aging times (Fig. 7a). Sample AT1, which was aged at 645 °C for 1 h, had almost the same magnetic properties as sample AT2, which was aged at 645 °C for 1 h and then at 620 °C for an additional hour. The HAADF data showed that decomposition occurred in sample AT1. Extending the aging time for another hour at the same temperature would have resulted in more decomposition. For sample AT2, however, we used a lower temperature for further aging treatment, expecting it to slow down or even stop the diffusion necessary for decomposition. The corresponding HAADF data, however, showed that the additional aging time of one hour resulted in more decomposition at the lower temperature in sample AT2 than had already occurred at the higher temperature in sample AT1. By analyzing both magnetic properties and HAADF, we concluded that the additional spinodal decomposition in sample AT2 had a limited effect on the magnetic properties. From samples AT2 to AT5, as spinodal decomposition progressed further at lower and lower temperatures, the values of both coercivity and remanence exhibited a significant increase, but from samples AT5 to AT6, coercivity increased while remanence decreased (Fig. 7b).

4. Discussion

4.1. Analysis of magnetic properties based on first-principles calculations

Spinodal decomposition is a solid-state phase transition that is known to be linked to the magnetic properties of materials [17-19,47]. These properties are closely related to such characteristics as the electronic DOS and magnetic moments of the elements [48,49]. Using both experimental methods and first-principles calculations, we investigated how the addition of Mo to the FeCrCo alloy affected the evolution of these two characteristics at various stages of spinodal decomposition.

Based on the crystal structures and compositions of the two phases acquired from XRD and STEM-EDS analyses, we calculated the partial

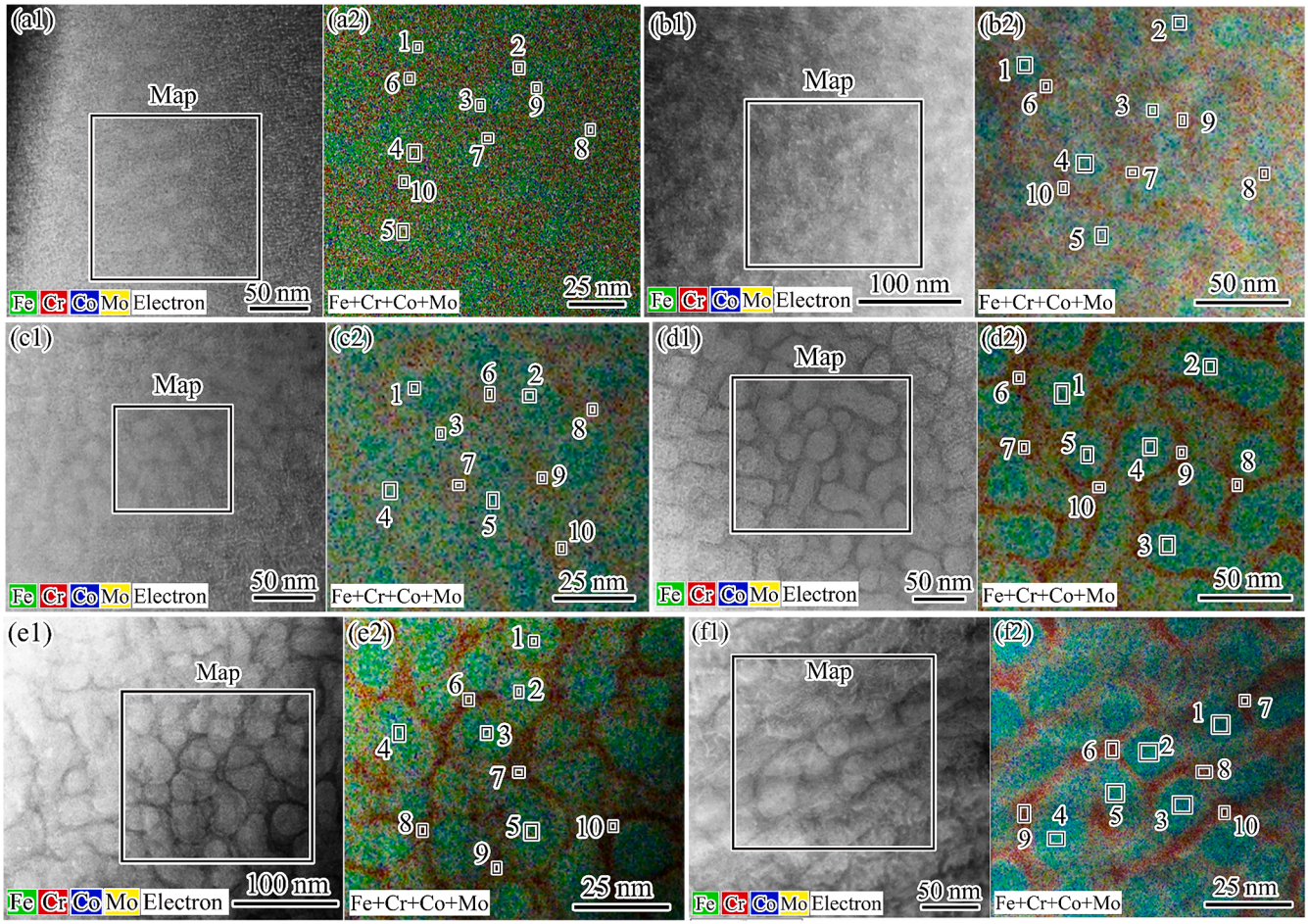

Fig. 3. Analysis of compositions of the α_1 and α_2 phases in samples AT1–AT6. (a1–f1) HAADF images. The large superimposed squares represent the areas subjected to EDS mapping. (a2–f2) EDS maps of Fe (Green), Cr (Red), Co (Blue), and Mo (Yellow) in samples AT1–AT6. Sub-maps extracted from the acquired STEM-EDS mapping areas (as indicated by small squares with numbers) were used to represent the areas subjected to quantitative composition analyses of the α_1 and α_2 phases (Fig. 4).

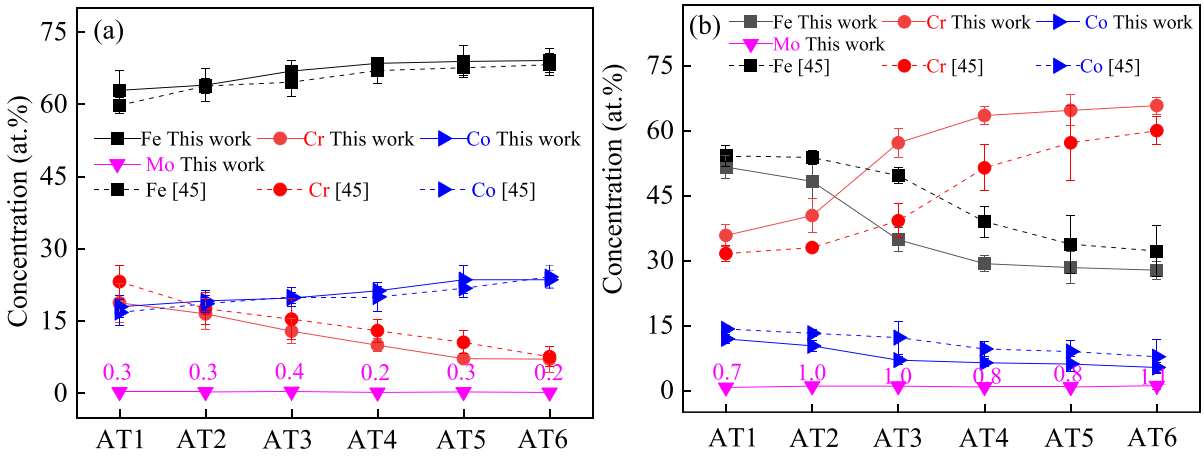

Fig. 4. Chemical compositions of the α_1 and α_2 phases in samples AT1–AT6, acquired from the STEM-EDS analysis of each sample. (a) α_1 phase. (b) α_2 phase. The compositions of the α_1 and α_2 phases in each non-alloyed sample have been included [45]. The error bars in some of the figures are extremely small to be visible.

DOS (pDOS) of Fe, Cr, Co, and Mo in both phases for samples AT1–AT6 (Fig. 8). For comparison, we separately calculated the pDOS of pure Fe, Cr, Co, and Mo (Fig. S4). The results indicated that for both pure Fe and Co, the spin-up distribution was higher than the spin-down distribution. In contrast, the spin distributions of pure Cr and Mo were fully symmetrical. These results confirm that both Fe and Co are magnetic, whereas Cr and Mo are non-magnetic. In the α_1 and α_2 phases, below the Fermi level, we also observed a significantly higher spin-up distribution than the spin-down distribution for both Fe and Co in samples AT1–AT6, indicating that Fe and Co play a substantial role in contributing to the magnetic moment for both phases. In samples AT1–AT6, the pDOS of Cr and Mo atoms in the α_1 and α_2 phases were relatively asymmetrical and

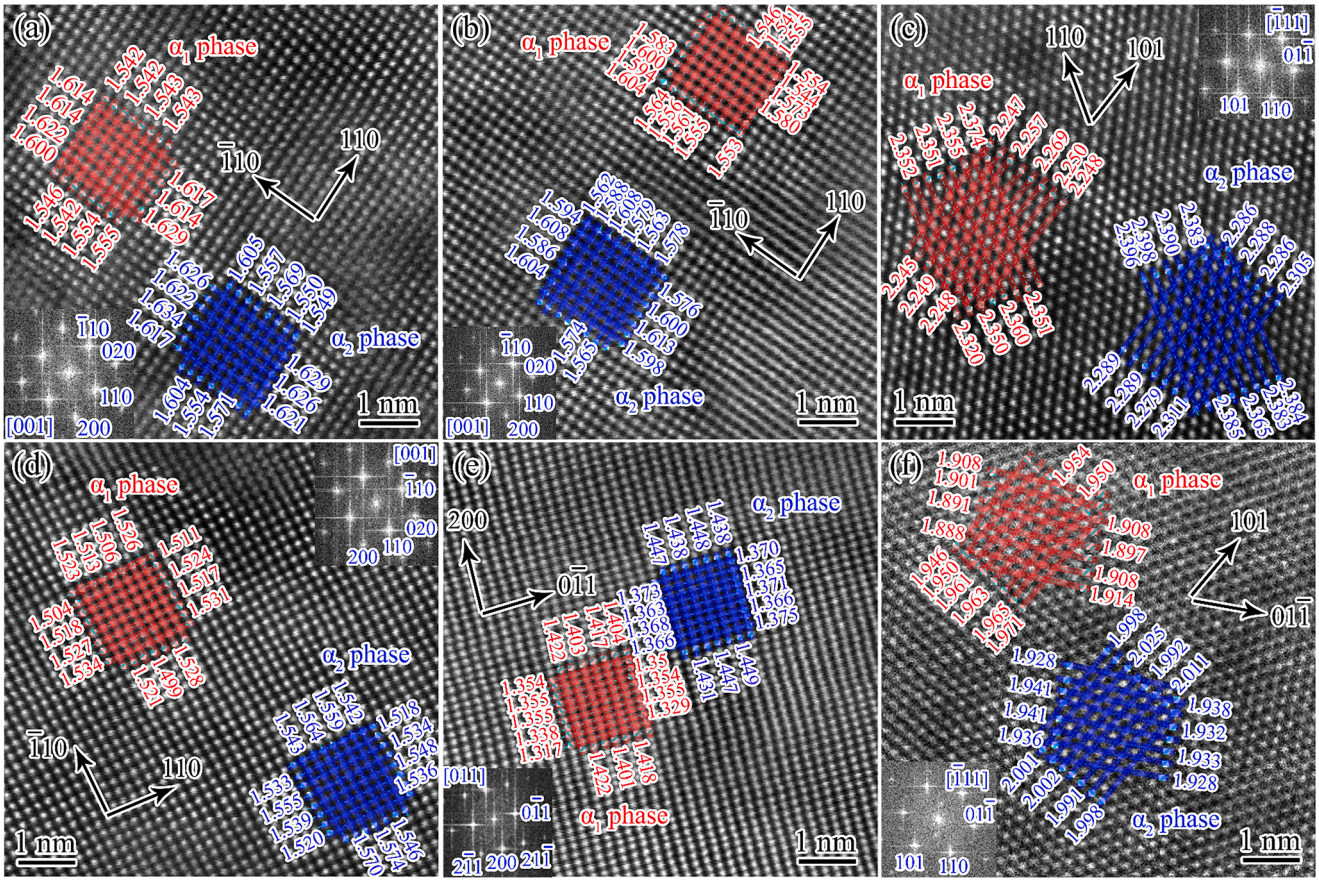

Fig. 5. Analysis of lattice spacing and lattice parameter of the α_1 and α_2 phases. (a-f) Atomic-scale STEM-HAADF images of AT1, AT2, AT3, AT4, AT5, and AT6, respectively. The inserts in figs. (a)-(f) are the corresponding FFT images. The values of lattice spacing in the α_1 phase are measured along red lines, while in the α_2 phase are measured along blue lines. Using these values, we calculate the average values of lattice parameter in the α_1 and α_2 phases for samples AT1-AT6 (Fig. 6).

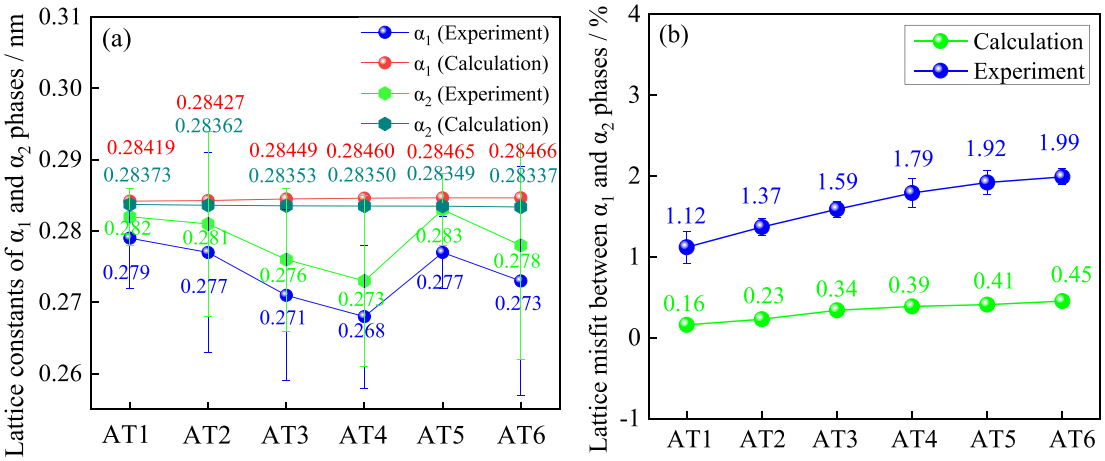

Fig. 6. Calculated and measured lattice constants of the α_1 and α_2 phases and the lattice mismatch between these two phases in samples AT1–AT6. (a) Lattice constant. (b) Lattice mismatch. The lattice mismatch (η) is calculated using the equation $\eta = \frac{2(a_1-a_2)}{(a_1+a_2)} \times 100\%$, where a_1 and a_2 are the lattice parameters of the α_1 and α_2 phases, respectively.

exhibited a more pronounced spin-down distribution than spin-up distribution, resulting in a reduction in the net magnetic moments of the α_1 and α_2 phases. This reduction occurred because of the antiparallel alignment between the magnetic moments of Cr and Mo and those of Fe and Co (Fig. 8). In addition, we found that the total pDOS of both α_1 and α_2 phases exhibited a substantially higher spin-up distribution than spin-down distribution in samples AT1–AT6, indicating that both the α_1 and α_2 phases are magnetic (Figs. 8e1 and 8e2).

To comprehend the changes that occurred in the saturation magnetization of the α_1 and α_2 phases as decomposition progressed, we calculated the magnetic moments of all atoms within these two phases in samples AT1–AT6 (Fig. 9). The calculated magnetic moments for any given atom of Co, Fe, Cr, or Mo were 1.66, 2.28, 1.07, or 0 μ_B, respectively (Fig. S4e). These values indicate that both Co and Fe are

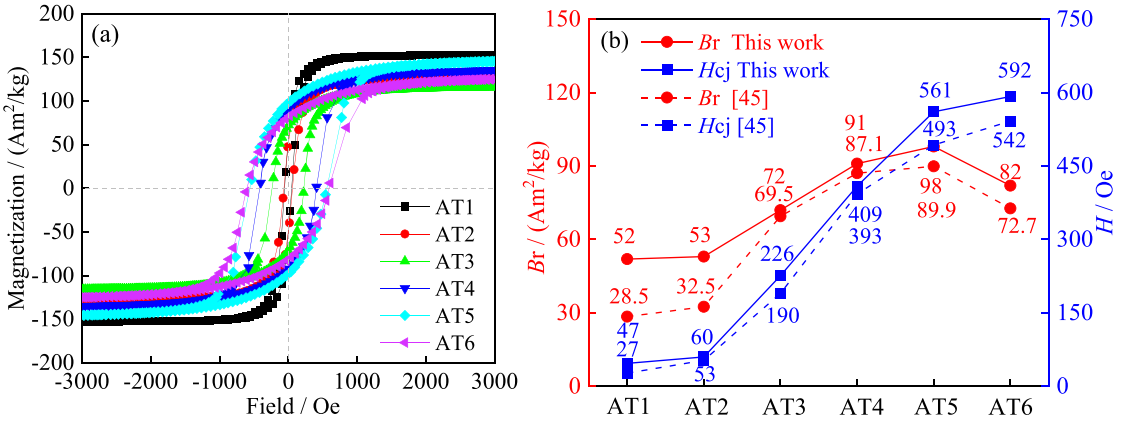

Fig. 7. Hysteresis loops and magnetic properties of samples AT1–AT6. (a) Hysteresis loops. We determined the saturation magnetization values of samples AT1–AT6 (Table 3). (b) Remanence (B_r) and coercivity (H_{cj}) values obtained by analyzing the curves shown in Fig. 7a. We have included the coercivity and remanence values of all non-alloyed samples in Fig. 7b [45].

ferromagnetic elements, whereas Mo is non-ferromagnetic. Notably, Cr is an antiferromagnetic element, indicating that the magnetic moment of each individual Cr atom is non-zero, even though the average magnetic moment of all the Cr atoms taken together is zero. Because the magnetic moment of any given atom can be influenced by nearby atoms of other elements, the values for the average magnetic moments in the alloying forms of Fe, Cr, Co, or Mo were different in both phases from those in the pure metals. In the α_1 phase, both Fe and Co exhibited higher average magnetic moments, even though the average magnetic moments of Cr and Mo atoms were antiparallel to those of Fe and Co atoms. This occurred as a result of the spin distribution of pDOS (Fig. 8). In the α_2 phase, by comparison, the average magnetic moments of Fe and Co exhibited higher values, just as they did in the α_1 phase, but, in samples AT1-AT6, the values in the α_2 phase were consistently lower than those in the α_1 phase. Based on the magnetic moment of each atom in the α_1 and α_2 phases (Fig. 9), we further calculated the total magnetic moments for both phases in samples AT1–AT6 (Fig. 10a). The calculations demonstrated that, in each sample, the total magnetic moment of the α_1 phase was higher than that of the α_2 phase, indicating that α_1 is a hard magnetic phase, whereas α_2 is a soft magnetic phase.

Based on first-principles calculations, we calculated the saturation magnetization values (in Am^2/kg) for the α_1 and α_2 phases of samples AT1–AT6 using Eq. (1) [49].

$$M_{s,\ \text{phase}} = \frac{\mu_{B,\ \text{supercell}}}{W_{\text{supercell}}} \tag{1}$$

where $\mu_{B,\text{supercell}}$ is the total magnetic moment of the supercell [unit: $\mu_B = 9.274 \times 10^{-24}$ (Am^2) (Bohr magneton)] and $W_{\text{supercell}}$ is the total atomic weight of the supercell. Based on the compositions of the α_1 and α_2 phases (Fig. 4), we calculated the total atomic weight for each phase in samples AT1–AT6. The total magnetic moments of the two phases in samples AT1–AT6 are shown in Fig. 10a. We also calculated the saturation magnetization of the α_1 and α_2 phases in samples AT1–AT6 (Fig. 10b), which showed that the saturation magnetization of the α_1 phase gradually increased, whereas that of the α_2 phase gradually decreased from samples AT1 to AT6.

4.2. Analysis of magnetic properties based on the experimental data

The magnetic property data for the Mo-alloyed samples AT1–AT6 demonstrated that, 1) from AT1 to AT5, both coercivity and remanence gradually increased as spinodal decomposition progressed (Fig. 7b) and 2) both coercivity and remanence of samples AT1–AT6 were enhanced after alloying with Mo. The addition of Mo may have contributed to the enhancement in magnetic properties by improving the compositions, sizes, and volumes of the α_1 and α_2 phases, as well as the difference in the composition between the two phases.

First-principles calculations of the total magnetic moment of the two phases showed that α_1 is a stronger ferromagnetic phase (Fig. 10a) than α_2, indicating that the composition, volume, and size of the α_1 phase are the key factors in determining the magnetic properties of the alloy. Among these factors, our previous research concluded that the composition of the α_1 phase was the key factor [45]. The distributions of pDOS of Fe, Cr, Co, and Mo in the α_1 phase showed that Fe and Co are ferromagnetic. In contrast, the magnetic moments of the Cr and Mo atoms were antiparallel to those of the Co and Fe atoms (Fig. 8). This indicates that the Fe + Co content controls the magnetic properties of the FeCoCrMo alloy.

Several research groups have found that, in magnetic alloys, the magnetic properties decrease with an increase in the size of the individual particles of the magnetic phase, and increase with an increase in the volume fraction of the magnetic phase as a whole [50-52]. Because the magnetic properties of spinodal alloys are mainly determined by the ferromagnetic α_1 phase, we used its microstructural parameters to estimate the coercivity and remanence values for samples AT1–AT6. Zhou et al., in their study of AlNiCo alloys, used Eq. (2) to estimate the remanence (B_r) [53]. Because the magnetic properties of both AlNiCo and our FeCrCoMo were improved by spinodal decomposition, we used the same equation to investigate the variation in B_r for samples AT1–AT6. The value of B_r can be determined using Eq. (2).

$$B_r = PC^{Fe+Co}M_S \tag{2}$$

where P is the volume fraction of the α_1 phase, C^{Fe+Co} is the concentration of (Fe + Co) in the α_1 phase, and M_S is the saturation magnetization of the alloy. According to the EDS (Fig. 4) and magnetic property (Fig. 7a) data, we acquired the concentration of Fe + Co in the α_1 phase and M_S for samples AT1–AT6 (Table 3). Combing of the volume fractions of the α_1 phase for samples AT1-AT6 (Fig. 2), we then calculated the values of Br for samples AT1-AT6, respectively (Table 3). The calculated data was consistent with the measured data (Fig. 7b). Thus, we conclude that the content of (Fe + Co) in the stronger ferromagnetic phase is the key factor in determining the remanence of the FeCrCoMo alloy.

For the ellipsoidal α_1 phase, other researchers used the following Eq. (3) to describe the value of coercivity for spinodal alloys [54].

$$H_{cj} = (N_b - N_a)p(1-p)\frac{(M_{s\alpha1} - M_{s\alpha2})^2}{M_s} \tag{3}$$

where $M_{s\alpha1}$ and $M_{s\alpha2}$ represent the saturation magnetizations of the α_1 and α_2 phases, respectively, N_a and N_b are the demagnetizing factors of α_1 particles along the a and b axes, respectively. In samples AT1–AT6,

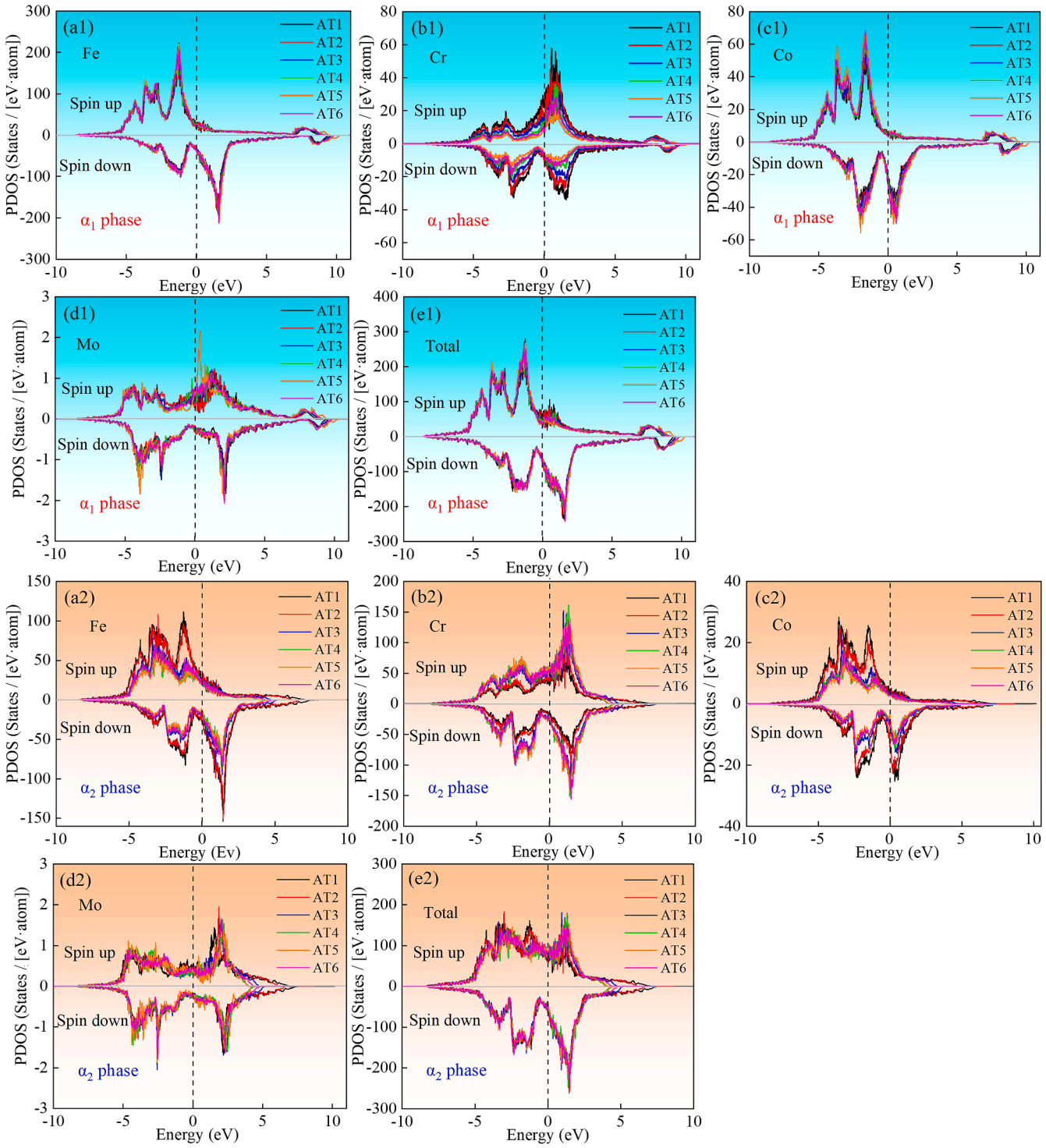

Fig. 8. First-principles computations results. Total pDOS of the α_1 and α_2 phases and pDOS of the Fe, Co, Cr, and Mo atoms in the α_1 and α_2 phases of samples AT1–AT6. (a1–d1) pDOS of the Fe, Co, Cr, and Mo atoms in the α_1 phase, respectively. (e1) Total DOS of the α_1 phase. (a2–d2) pDOS of the Fe, Co, Cr, and Mo atoms in the α_2 phase, respectively. (e2) Total DOS of the α_2 phase. The Fermi level is represented by the vertical dotted lines.

the shape of the α_1 phase was spherical (Fig. 2), the H_{cj} can be derived using Eq. (4).

$$H_{cj} = Np(1-p)\frac{(M_{s\alpha1} - M_{s\alpha2})^2}{M_s} \tag{4}$$

Since the values of N for all the AT1–AT6 samples were the same, and the volume percentage of the α_1 phase remained constant from samples AT3 to AT6, indicating that the coercivity was determined using the term: $(M_{s\alpha1} - M_{s\alpha2})^2/M_s$. We used $N = 1/3$ for our calculations. The values of saturation magnetization for samples AT1-AT6 indicated that coercivity is closely related to the saturation magnetization gap between the α_1 and α_2 phases (Table 3). Using first-principles calculations, we determined the values of saturation magnetization ($M_{s\alpha1}$ and $M_{s\alpha2}$) for both α_1 and α_2 phases, and we then calculated the difference between $M_{s\alpha1}$ and $M_{s\alpha2}$ for each of the six samples (Fig. 10b). Finally, we calculated the coercivity values: 0.8 Am^2/kg (77 Oe), 1.7 Am^2/kg (165 Oe),

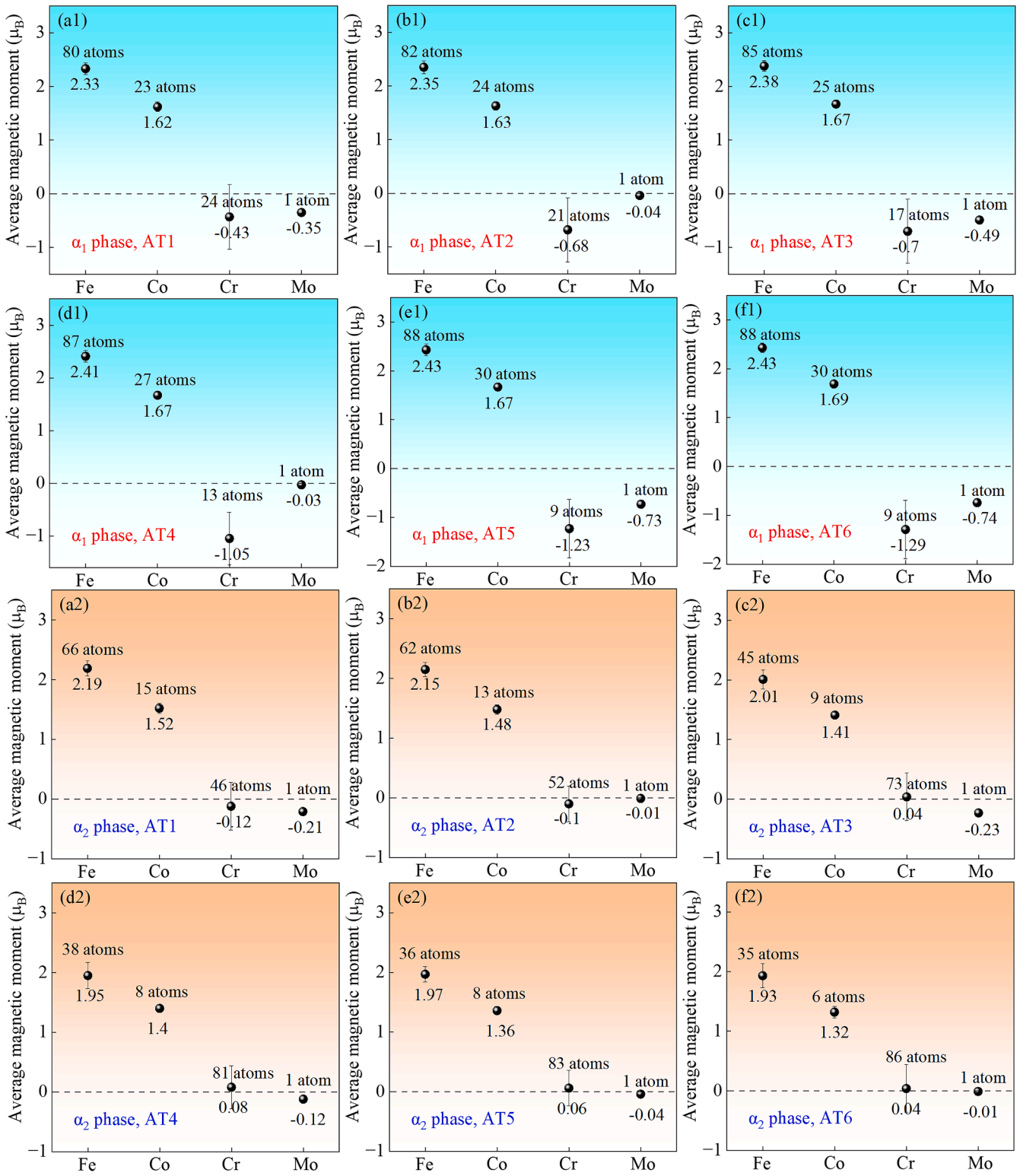

Fig. 9. First-principles computations results. Average magnetic moments of the Fe, Co, Cr, and Mo atoms in the α_1 and α_2 phases of samples AT1–AT6, as predicted from the calculations at 0 K. (a1)-(f1) Average magnetic moment in the α_1 phase of Samples AT1-AT6, respectively. (a2)-(f2) Average magnetic moment in the α_2 phase of Samples AT1-AT6, respectively. The error bars in some of the figures are extremely small to be visible.

5.4 Am^2/kg (532 Oe), 6.6 Am^2/kg (647 Oe), 7.7 Am^2/kg (761 Oe), and 9.7 Am^2/kg (956 Oe) for samples AT1-AT6, respectively. Both the calculated and measured results demonstrated that coercivity increased step by step from AT1 to AT6. Thus we concluded that the magnetic moment gap between α_1 and α_2 phases played a dominant role in determining coercivity.

Several research groups have reported that stress can influence the distribution of electron spin, suggesting a strong correlation between the lattice strain and magnetic properties [55-57]. In this study, we used a combination of atomic resolution HAADF-STEM images and the Strain++ software to calculate the coherency strain distribution between the FeCo-rich α_1 and Cr-rich α_2 phases in samples AT2–AT5. The

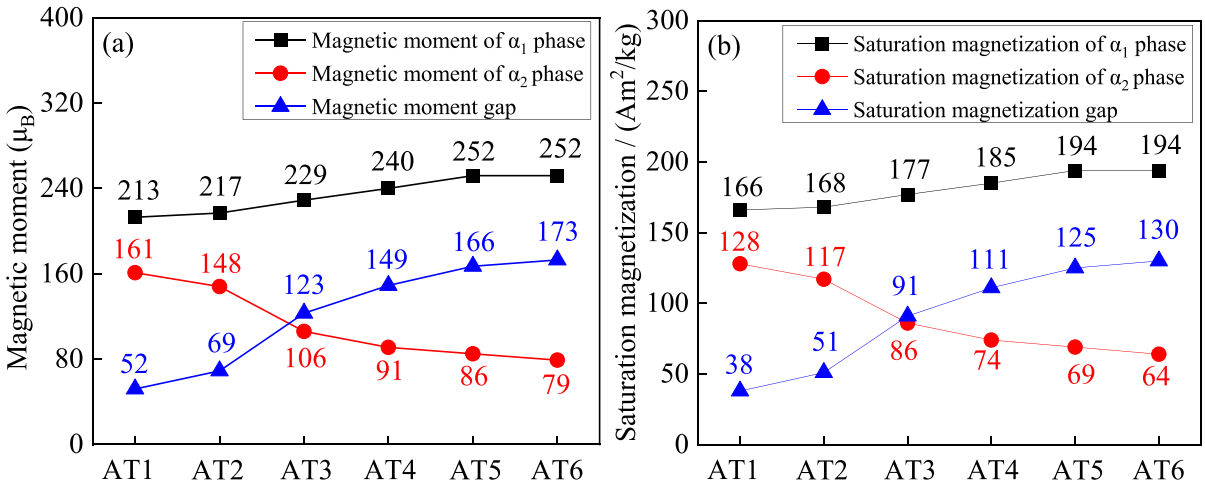

Fig. 10. Calculated magnetic properties of the α_1 and α_2 phases in the samples AT1–AT6. (a) Magnetic moments of the two phases and magnetic moment gap between them in samples AT1–AT6, as predicted from the first-principles calculations at 0 K. (b) Saturation magnetization of the two phases and the saturation magnetization gap between them in samples AT1–AT6 based on the first-principles calculations.

Table 3
Measured and calculated properties of samples (AT1-AT6).

Sample	Measured properties		Calculated properties		
	Ms / Am^2/kg	$C_{\alpha1(Co+Fe)}$ / at %	*Br* / Am^2/kg	*Hcj* / Oe	*e* / erg/cm^3
AT1	152	80.9	55	77	1.86×10^6
AT2	127	83.2	59	165	2.28×10^6
AT3	116	86.7	65	532	2.64×10^6
AT4	140	89.8	83	647	2.98×10^6
AT5	151	92.5	92	761	3.19×10^6
AT6	130	92.7	79	956	3.31×10^6

results indicated that coherency strain was induced by spinodal decomposition in samples AT2–AT5 (Fig. 11). Using the lattice constant values of the α_1 and α_2 phases, which were calculated based on the first-principles calculations and experimental measurements (Section 3.1), we further calculated the lattice mismatch between the two phases for samples AT1–AT6 (Fig. 6). Both calculation methods showed that the lattice mismatch increased step by step from samples AT1 to AT6, leading to a corresponding increase in the magnetic properties. It was also found that an increase in the lattice strain induced magnetocrystalline anisotropy, resulting in an enhancement in the magnetic properties [58-61]. The magnetocrystalline anisotropy energy can be estimated using Eq. (5) [62].

$$e = 3\lambda\sigma/2 \tag{5}$$

where λ is the magnetostriction coefficient, we measured the value of magnetostriction coefficient for 6.4Fe29Cr14Co0.6Mo alloy is 48×10^{-6}. The stress, σ, is derived from Eq. (6).

$$\sigma = Y\varepsilon \tag{6}$$

where Y is the Young's modulus, and ε is the strain between the α_1 and α_2 phases. The Young's moduli for Fe, Co, Cr, and Mo are 211, 209, 279, and 329 GPa, respectively, and we estimated the Young's modulus was 231 GPa for the 56.4Fe29Cr14Co0.6Mo alloy. According to the values of strain measured from the HAADF images (Fig. 6), we then calculated the values of *e*, which is a misfit between α_1 and α_2, for samples AT1-AT6, respectively (Table 3). Because the lattice constants of α_2 and α_1 smaller than that of Mo (0.3147 nm), Mo addition increased the lattice constant of both phases. Our chemistry analyses showed that Mo content ratio in α_2 over α_1 phase increased from 2.3 to 5.5, leading to more increase of lattice constant increase in α_2 than α_1. Mo addition therefore increased the values of *e*. This increase was enhanced as aging progressed and contributed to a gradually increased magnetocrystalline-anisotropy-energy from samples AT1 to AT6, resulting in a corresponding increase in magnetic properties.

Comparing with non-alloyed samples, the addition of Mo resulted in an enhancement in both coercivity and remanence for each sample. Samples AT1–AT6 exhibited an increase of 74 %, 13 %, 19 %, 4 %, 14 %, and 9 % in coercivity and an increase of 82 %, 63 %, 4 %, 4 %, 9 %, and 13 % in remanence, respectively (Fig. 7b). These enhancements in the magnetic properties can be potentially attributed to the improvement in the compositions, sizes, and volume fractions of the α_1 and α_2 phases, as well as the lattice strain influenced by Mo alloying. The distributions of pDOS of Mo atoms in the α_1 and α_2 phases showed that the magnetic moment of Mo atom was antiparallel to those of Fe and Co atoms, which should decrease magnetic properties for Samples AT1-AT6. However, both the coercivity and remanence were enhanced for each sample, we attributed these increases to four factors. 1) The volume of the α_1 phase increased by 22 %, 2 %, 7 %, 7 %, 8 %, and 7 % for samples AT1–AT6, respectively (Fig. 2g); 2) The Fe + Co content in the α_1 phase increased by 5.6 %, 1.0 %, 2.5 %, 3.2 %, 0.1 %, and 5.3 % for samples AT1–AT6, respectively (Fig. 4a); 3) The intensity of composition fluctuation between the α_1 and α_2 phases was enhanced for each Mo-alloyed sample, leading to an increase in the saturation magnetization difference between the two phases of each sample; 4) The lattice strain was improved by adding Mo in samples AT1-AT6. Because the atomic radius of Mo (139pm) is higher than either of Fe (126pm), Cr (128pm) or Co (125pm), leading to the lattice misalignments were introduced in each sample of AT2-AT5 (Fig. 12). These lattice misalignments generated additional internal stress, leading to an increase in the magnetocrystalline anisotropy, and resulting in a corresponding increase in both the coercivity and remanence for each sample. In addition, we tested the hardness for samples AT1-AT6 (Fig. S5). Comparing with these non-alloyed samples [45], the addition of Mo resulted in an enhancement in hardness for each sample, indicating that the strain was enhanced by Mo addition.

4.3. Impact of magnetic domain on the magnetic properties

Previous studies have reported a significant correlation between the magnetic properties of alloys and the exchange-coupling interactions between their soft and hard phases. The strength of these interactions depends on various factors, such as the size, volume, and composition of the respective phases [63-65]. Some researchers used magnetic annealing to refine the soft α-Fe phase in $Nd_2Fe_{14}B$/α-Fe-type

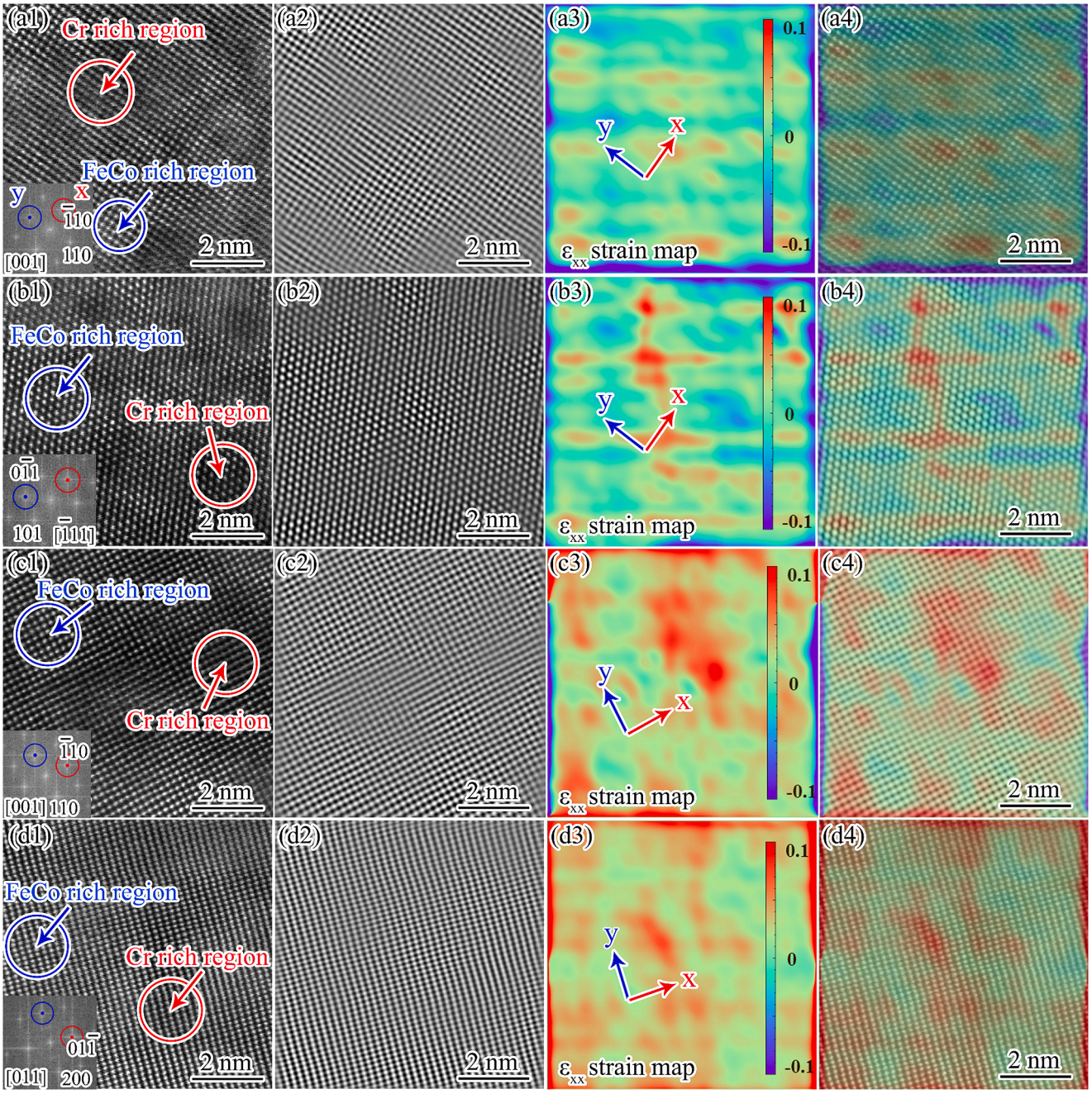

Fig. 11. Analysis of coherent strain distribution between the (Fe-Co)-rich α_1 and Cr-rich α_2 phases in samples AT2–AT5. (a1–d1) Atomic-scale HAADF-STEM images of samples AT2–AT5, respectively. The inserts are the corresponding FFT images. (a2–d2) Inverse FFT images of (a1–d1). (a3–d3) GPA strain maps (ε_{xx}) calculated along the $\bar{1}10$ and $\bar{1}10$ directions of (a1) and (c1), the $0\bar{1}1$ and $\bar{1}0\bar{1}$ directions of (b1), and the $\bar{2}00$ and $01\bar{1}$ directions of (d1). All the directions are indicated in the inserted FFT images in Figs. (a1–d1). (a4–d4) Overlapping of HAADF-STEM images (a1–d1) with the ε_{xx} strain maps (a2–d2), respectively. These images show the atomic structure and internal strain variations locally near the interface of the two phases. The red regions indicate the positive strain, whereas the blue regions indicate the negative strain.

nanocomposites. This refinement enhanced the exchange-coupling interactions, resulting in a significant increase in the magnetic properties [51]. Similarly, refinement of the hard phase during the manufacturing of SmCo/NdFeB hybrid magnets led to an increase in exchange-coupling interactions, which resulted in an improvement in the magnetic properties [12]. In our studies, first-principles calculations indicated that the (Fe + Co)-rich α_1 phase (which has a higher magnetic moment) is the hard phase, whereas the Cr-rich α_2 phase (which has a lower magnetic moment) is the soft phase (Fig. 10a). To show that the exchange interactions between the two phases existed in our samples AT1–AT6, using the rule of mixtures, the magnetic moments of Fe + Co in the α_1 phase were determined to be 221, 227, 235, 243, 250, and 250 μ_B for samples AT1–AT6, respectively, based on the magnetic moments of Fe (2.28 μ_B) and Co (1.66 μ_B), and the contents of Fe and Co in the α_1 and α_2 phases (Fig. S4e and Fig. 4). In contrast, the magnetic moments of Fe + Co in the α_2 phase were 175, 163, 118, 100, 94, and 90 μ_B for samples AT1–AT6, respectively. From first-principles calculations, we calculated the magnetic moments of Fe + Co in the α_1 phase were 223, 232, 244, 255, 264, and 265 μ_B for samples AT1–AT6, respectively. In contrast, the magnetic moments of Fe + Co in the α_2 phase were 167, 153, 103, 85, 82, and 75 μ_B for samples AT1–AT6, respectively. Comparing with the rule of mixture calculation, we found that the magnetic moment

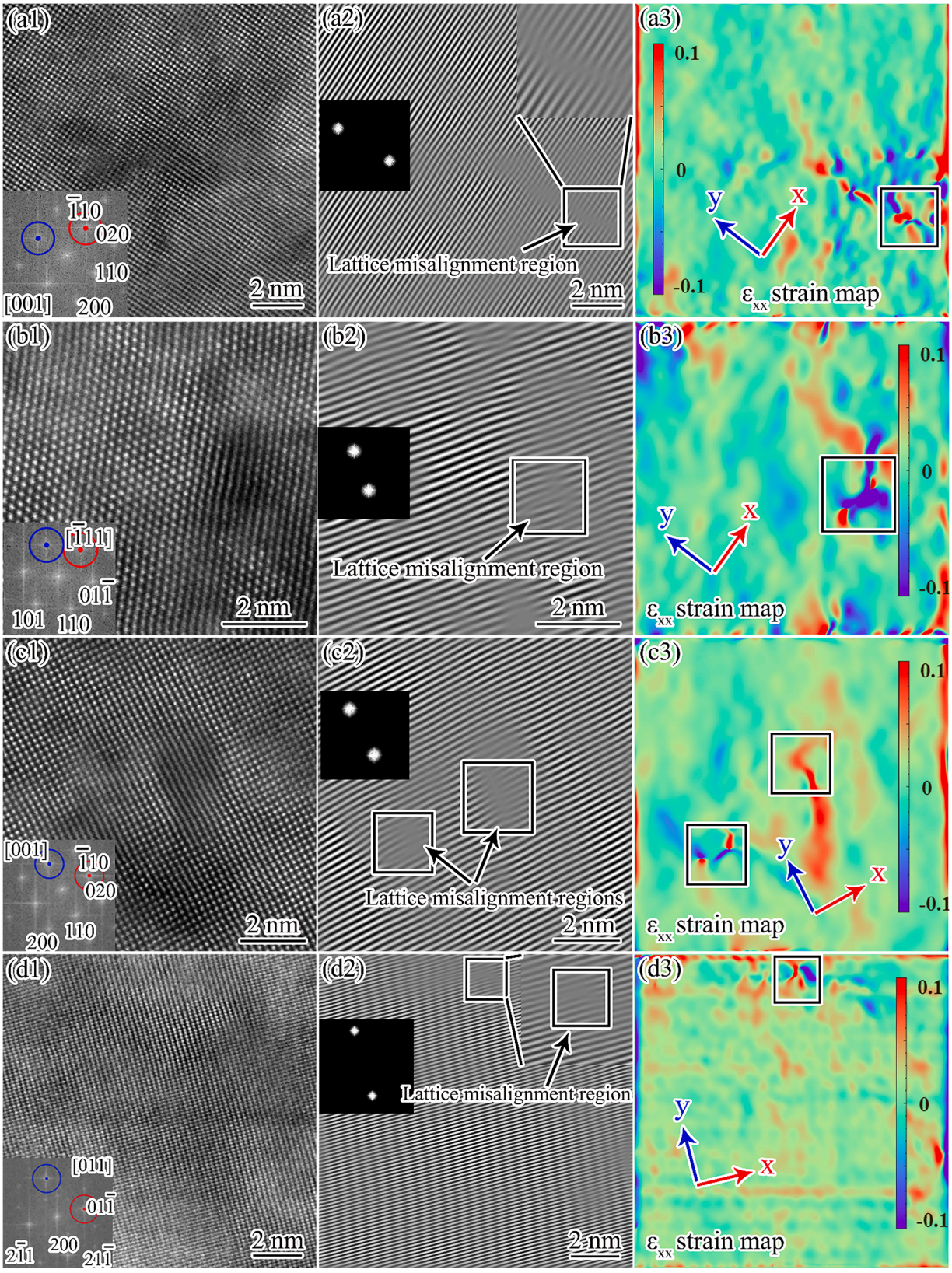

Fig. 12. Analysis of lattice misalignment in samples AT2–AT5. (a1–d1) Atomic-scale HAADF-STEM images of the samples AT2–AT, respectively. The insets are the corresponding FFT images. (a2–d2) Corresponding inverse FFT images of (a1–d1), which are obtained from the FFT images shown as insets in Figs. (a2–d2). The lattice misalignment regions are indicated by rectangles. (a3–d3) GPA strain maps (ε_{xx}) calculated along the $\bar{1}\bar{1}0$ and $\bar{1}10$ directions of (a1) and (c1), $\bar{1}\bar{1}0$ and $\bar{1}0\bar{1}$ directions of (b1), $\bar{2}00$ and $01\bar{1}$ directions of (d1). All directions are indicated in the inserted FFT images shown in Figs. (a1–d1). The compression and extension strain fields around the lattice misalignment are shown in the rectangles.

difference of (Fe + Co) between the two phases calculated from the first-principles calculations increased by 21.7 %, 23.4 %, 20.5 %, 18.8 %, 16.7 %, and 18.8 % for samples AT1–AT6, respectively, indicating the existence of exchange-coupling interactions between the hard α_1 and soft α_2 phases.

In samples AT3–AT6, the volume fraction of the α_1 phase remained constant, thus limiting the impact of volume fraction on exchange coupling. This result is similar to that reported by Kakeshita et al. [66] and Zhou et al. [18]. In samples AT1–AT6, the α_1 phase gradually coarsened. According to previous studies, this should have decreased the exchange coupling. In fact, magnetic properties gradually increased from samples AT1 to AT6. We attributed this increase to the enhanced exchange coupling introduced by increased composition fluctuations between the soft α_2 and hard α_1 phases. According to Eq. (3), the coercivity is determined by the saturation magnetization gap between the soft and hard phases. The saturation magnetization gap itself is determined by the compositional difference between the two phases. Based on the first-principles calculations, we observed an increase in the saturation magnetization gap between the two phases from samples AT1 to AT6 (Fig. 10b). This suggests that the exchange coupling was enhanced from samples AT1 to AT6. It has been previously shown that the magnetic properties can be significantly affected by the coupling interaction between magnetic domains. Furthermore, the morphology and size of the magnetic domains are closely related to the exchange coupling between the soft and hard phases and the morphologies of the respective phases [67-69]. In sample AT1, which has a lower saturation magnetization difference, the morphology of the domains resembled a maze network (Fig. 13a). As the saturation magnetization difference increased, the shape of the magnetic domains shifted from a maze to a sphere (as in the case of samples AT5 and AT6 shown in Fig. 13). Using MFM images, we measured the widths of the magnetic domains for samples AT1–AT6. The results indicated that the width of the domains gradually decreased from samples AT1 to AT5. This suggests that additional exchange interactions between the magnetic domains were introduced in the samples, leading to a corresponding increase in both coercivity and remanence in samples AT1–AT5. From samples AT5 to Sample AT6, however, the width of the domains increased slightly, leading to a decrease in remanence (Fig. 13).

4.4. Comparison between our work and previous research

Among all the aged samples, sample AT6 showed the best combination of hardness, coercivity, remanence, and saturation magnetization. Alloying with Mo increased all of these values in the case of sample AT6 by 10.1 %, 9.2 %, 12.3 %, and 14.0 %, respectively. When we compared these values with those of Fe, Cr, and Co contained high-entropy alloys (HEAs) studied by other researchers, we found that the saturation magnetization of sample AT6 was lower than that of $Al_{0.1}(Fe_{1.6}CoCr_{0.4}Mn)_{0.9}$ [49] and its hardness was lower than that of $CoCrFeNiTiAl_x$ [70]. Although the values of saturation magnetization and hardness for the previously reported HEAs were higher than those for sample AT6, their remanence values were excessively low to allow their use as permanent magnet materials. Sample AT6 surpassed all these previously reported HEAs in terms of coercivity and remanence (Table 4).

When we compared these values with those of FeCrCo-based alloys studied by other researchers. We found that the coercivity of sample AT6 was higher than that of $Fe_{60}Cr_{30}Co_{10}$ [71] and $Fe_{66}Cr_{30}Co_6$ [32].

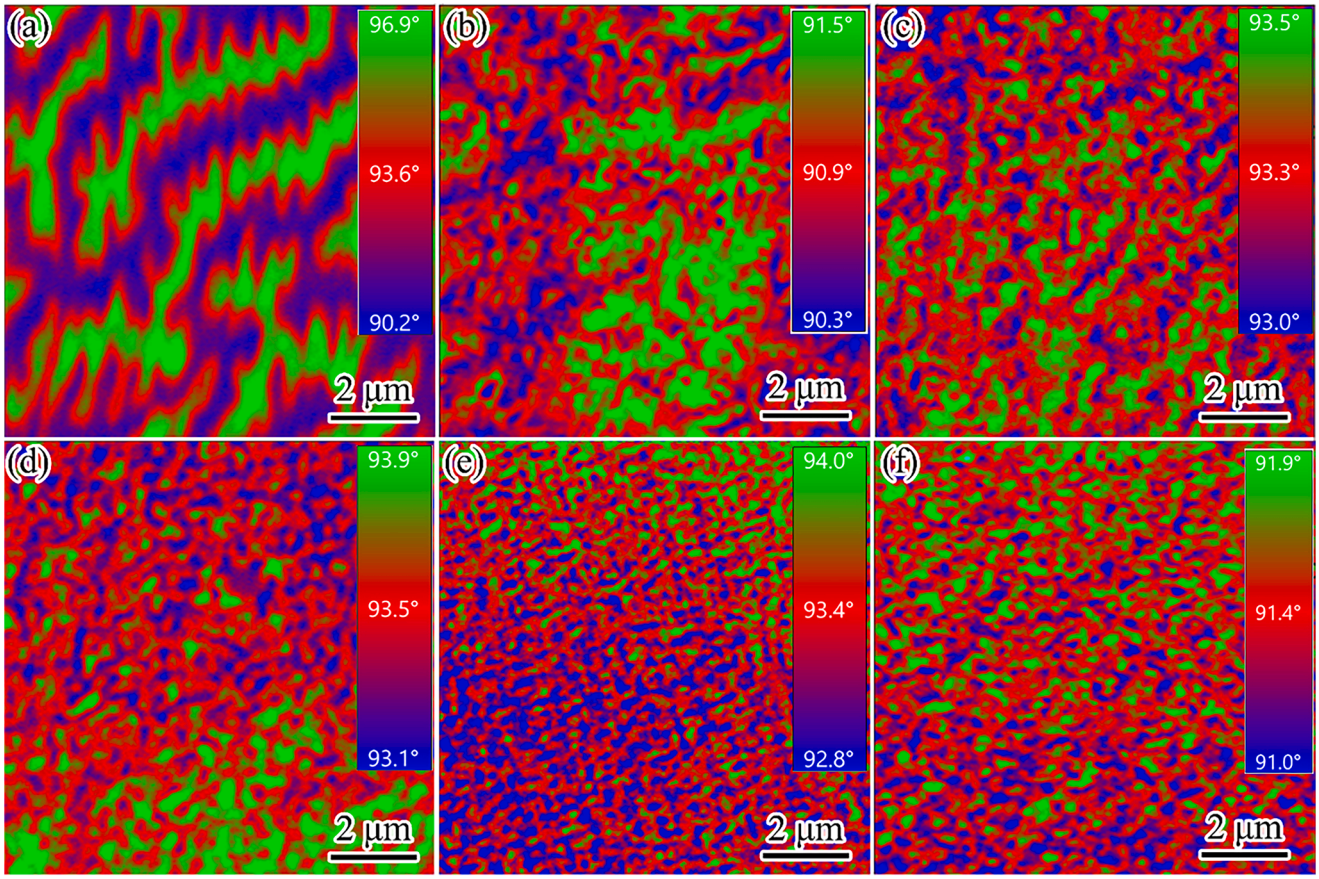

Fig. 13. MFM images showing the development of the magnetic domain structure in samples AT1–AT6. (a) AT1, (b) AT2, (c) AT3, (d) AT4, (e) AT5, and (f) AT6. The inserts shows the angles of the magnetic domains. The domain widths measured from the MFM images are 467 ± 80, 323 ± 69, 225 ± 46, 209 ± 52, 131 ± 37, and 143 ± 42 nm for the samples AT1–AT6, respectively.

Table 4
Comparison of properties of Sample AT6 and those of others.

Alloys	Coercivity/Oe	Remanence/Am^2/kg	Saturation magnetization/Am^2/kg	Hardness/HV
$Fe_{56.4}Cr_{29}Co_{14}Mo_{0.6}$	592	82	130	447
$Fe_{57}Cr_{29}Co_{14}$ [45]	542	73	114	406
$Fe_{60}Cr_{30}Co_{10}$ [71]	60–180	–	–	360
$Fe_{61}Cr_{25}Co_{11}Si_3$ [44]	158–742	34–88	118–153	–
$Fe_{53}Cr_{30}Co_{14}Mo_2Ti_1$ [37]	760	77	157	–
$Fe_{46}Cr_{31}Co_{21}Si_2$ [15]	660	98	–	–
$Fe_{53}Cr_{34}Co_{11}Si_2$ [72]	640	130	–	–
$Fe_{45}Cr_{33}Co_{22}$ [14]	660	116	–	–
$Fe_{64}Cr_{30}Co_6$ [32]	340	92	128	–
$Fe_{47}Cr_{30}Co_{21}Si_2$ [73]	510	126	–	–
$Fe_{42}Cr_{32}Co_{24}Mo_2$-[14]	780	115	–	–
$Fe_{51.4}Cr_{32}Co_{14}Mo_2Ti_{0.6}$ [35]	754	83	95	–
$Fe_{52}Cr_{30}Co_{14}Mo_2Ti_2$ [39]	990	113	136	–
$Co_{35}Cr_5Fe_{10}Ni_{30}Ti_{20}$ [74]	1.7	extremely low	78	–
$AlCo_xCr_{1-x}FeNi$ [75]	9–149	extremely low	18–117	–
$Al_{0.1}(Fe_{1+x}CoCr_{1-x}Mn)_{0.9}$ [49]	8–13	extremely low	86–136	–
CoCrFeNiCuAl [76]	45	extremely low	38	–
$CoCrFeNiTiAl_x$ [70]	20–285	extremely low	0.76–14.78	603–735
FeCoNiCr [77]	23	extremely low	30.7	–
FeCoNiCrCu [77]	33	extremely low	32.7	–

"–" means not detectable.

However, both the coercivity and remanence were significantly increased for the $Fe_{46}Cr_{31}Co_{21}Si_2$ [15] and $Fe_{53}Cr_{34}Co_{11}Si_2$ [72] alloys, which were synthesized by a combination of deformation. Similarly, a notable enhancement in both coercivity and remanence was found in the $Fe_{45}Cr_{33}Co_{22}$ [14], $Fe_{42}Cr_{32}Co_{24}Mo_2$ [14], $Fe_{64}Cr_{30}Co_6$ [32], $Fe_{51.4}Cr_{32}Co_{14}Mo_2Ti_{0.6}$ [35], $Fe_{52}Cr_{30}Co_{14}Mo_2Ti_2$ [39], and $Fe_{47}Cr_{30}Co_{21}Si_2$ [73] alloys, which were subjected to an aging treatment accompanied by the application of a magnetic field (Table 4). Because of this, we speculate that the coercivity, remanence, and saturation magnetization of our samples can be further improved by appropriate deformation and thermomagnetic treatments. This study could provide theoretical guidance for designing advanced magnetic materials and could be particularly useful for incorporating spinodal decomposition in the process.

5. Conclusions

We investigated the effect of Mo alloying on the correlations among microstructure, magnetic properties, and hardness in an FeCrCo alloy. The results can be summarized as follows:

1. EDS analyses showed that Mo was enriched in the α_2 phase, which resulted in a larger lattice constant than that for the α_1 phase. The introduction of lattice distortion by alloying with Mo led to a greater lattice strain between the α_1 and α_2 phases during each stage of spinodal decomposition, resulting in a corresponding enhancement in the magnetic properties and hardness.
2. First-principles calculations showed that, as spinodal decomposition progressed, the saturation magnetization of the α_1 phase gradually increased while that of the α_2 phase gradually decreased. In our Mo-alloyed FeCrCo alloy, the expanding gap in the saturation magnetization between the α_1 and α_2 phases might have contributed to a corresponding increase in coercivity.
3. As spinodal decomposition progressed, the width of the magnetic domain gradually decreased. This resulted in an increase in the exchange interactions between the adjacent magnetic domains, thus leading to a corresponding increase in both coercivity and remanence. At the last stage of the spinodal decomposition, however, there was a slight increase in the domain width, which led to a corresponding decrease in the remanence.
4. In all stages of the spinodal-decomposed samples, alloying with Mo increased their hardness, coercivity, and remanence values. We attributed these increases to three factors: 1) a greater volume percentage of the α_1 phase, 2) a greater compositional gap between the α_1 and α_2 phases, and 3) an increase in the lattice mismatch between the two phases.

CRediT authorship contribution statement

Zhaolong Xiang: Conceptualization, Writing – original draft, Writing – review & editing, Methodology, Visualization, Investigation. **Engang Wang:** Conceptualization, Resources, Methodology, Supervision. **Tao Wang:** Writing – review & editing. **Bailing An:** Validation, Investigation. **Yan Xin:** Resources, Validation, Investigation. **Jun Lu:** Resources, Validation, Investigation. **Rongmei Niu:** Resources, Validation, Investigation. **Zhishan Mi:** First-principles calculations. **Wenqing Wei:** Resources, Validation. **Baode Sun:** Resources, Validation. **Ke Han:** Conceptualization, Resources, Methodology, Writing – review & editing, Supervision, Project administration, Funding acquisition, Validation. **Xi Li:** Resources, Methodology, Editing, Supervision, Project administration, Funding acquisition, Validation.

Declaration of competing interest

The authors declare that they have no known competing financial interests or personal relationships that could have appeared to influence the work reported in this paper.

Acknowledgment

This work was supported by the National Natural Science Foundation of China (52174365) and National Key Research and Development Program of China (2023YFB3506701, 2022YFB3706801). A portion of this work was performed at the National High Magnetic Field Laboratory (NHMFL), which is supported by National Science Foundation (Cooperative Agreement No DMR-1644779, and DMR-2128556) and the State of Florida. We thank Mary Tyler for editing. Zhaolong Xiang was supported by the China Scholarship Council (CSC) during his studies at NHMFL.

Supplementary materials

Supplementary material associated with this article can be found, in the online version, at doi:10.1016/j.actamat.2024.120388.

References

[1] S.U. Rehman, C. Wei, Q. Huang, Q. Jiang, A. ul Haq, J. Wang, Z. Zhong, Tailoring the microstructure, magnetic properties and interaction mechanisms of Alnico-Ta alloys by magnetic field treatment, J. Alloys Compd. (2020) 157586.

[2] S. Motozuka, Y. Mako, H. Sato, H. Hojo, Y. Okazaki, Effect of lubricant milling aids on the recrystallization behavior and magnetic properties of ball-milled iron powders having (001) fiber texture for soft magnetic composite, J. Magn. Magn. Mater. 521 (2021) 167548.

[3] X. Tang, H. Sepehri-Amin, M. Matsumoto, T. Ohkubo, K. Hono, Role of Co on the magnetic properties of Ce-substituted Nd-Fe-B hot-deformed magnets, Acta Mater. 175 (2019) 1–10.

[4] D.R. Brown, K. Han, T. Siegrist, Hard magnetic properties observed in bulk $Mn_{1-x}Ga_x$, J. Appl. Phys. 115 (2014) 17A723.

[5] T. Yomogita, S. Okamoto, N. Kikuchi, O. Kitakami, H. Sepehri-Amin, Y. K. Takahashi, T. Ohkubo, K. Hono, K. Hioki, A. Hattori, Direct detection and stochastic analysis on thermally activated domain-wall depinning events in micropatterned Nd-Fe-B hot-deformed magnets, Acta Mater. 201 (2020) 7–13.

[6] T. Song, X. Tang, W. Yin, J. Ju, Z. Wang, Q. Liu, Y. Tang, R. Chen, A. Yan, Magnetic properties improvement of hot-deformed Nd–Fe–B permanent magnets by Pr–Cu eutectic pre-diffusion process, Acta Mater. 174 (2019) 332–341.

[7] A.K. Pathak, M. Khan, K.A. Gschneidner, R.W. McCallum, L. Zhou, K. Sun, K. W. Dennis, C. Zhou, F.E. Pinkerton, M.J. Kramer, V.K. Pecharsky, Cerium: an unlikely replacement of dysprosium in high performance Nd-Fe-B permanent magnets, Adv. Mater. 27 (2015) 2663–2667.

[8] W.B. Cui, Y.K. Takahashi, K. Hono, Microstructure optimization to achieve high coercivity in anisotropic Nd-Fe-B thin films, Acta Mater 59 (2011) 7768–7775.

[9] Y.H. Hou, Y.L. Wang, Y.L. Huang, Y. Wang, S. Li, S.C. Ma, Z.W. Liu, D.C. Zeng, L. Z. Zhao, Z.C. Zhong, Effects of Nd-rich phase on the improved properties and recoil loops for hot deformed Nd-Fe-B magnets, Acta Mater. 115 (2016) 385–391.

[10] O. Gutfleisch, K.H. Müller, K. Khlopkov, M. Wolf, A. Yan, R. Schäfer, T. Gemming, L. Schultz, Evolution of magnetic domain structures and coercivity in high-performance SmCo 2:17-type permanent magnets, Acta Mater. 54 (2006) 997–1008.

[11] B. Cui, X. Liu, A.H. King, G. Ouyang, C.I. Nlebedim, J. Cui, Overcoming mechanical fragility in Sm-Co permanent magnet materials, Acta Mater. 196 (2020) 528–538.

[12] D. Wang, N. Poudyal, C. Rong, Y. Zhang, M.J. Kramer, J.Ping Liu, Exchange-coupled nanoscale SmCo/NdFeB hybrid magnets, J. Magn. Magn. Mater. 324 (2012) 2836–2839.

[13] Q. Wang, L. Zheng, S. An, T. Zhang, C. Jiang, Thermal stability of surface modified Sm_2Co_{17}-type high temperature magnets, J. Magn. Magn. Mater. 331 (2013) 245–249.

[14] H. Kaneko, M. Homma, K. Nakamura, New Ductile Permanent Magnet of Fe-Cr-Co System, AIP Conf. Proc. 5 (1972) 1088–1092.

[15] H. Kaneko, M. Homma, M. Okada, S. Nakamura, N. Ikuta, Fe-Cr-Co ductile magnet with (BH)max=8 MGOe, AIP Conf. Proc. 620 (1976) 620–621.

[16] H. Zijlstra, Trends in permanent magnet material development, IEEE Trans. Magn. 14 (1978) 661–664.

[17] A. Hütten, G. Reiss, W. Saikaly, G. Thomas, Origin of giant magnetoresistance in conventional AlNiCo5 magnets, Acta Mater. 49 (2001) 827–835.

[18] L. Zhou, W. Tang, L.Q. Ke, W. Guo, J.D. Poplawsky, I.E. Anderson, M.J. Kramer, Microstructural and magnetic property evolution with different heat-treatment conditions in an alnico alloy, Acta Mater. 133 (2017) 73–80.

[19] L. Zhou, W. Guo, J.D. Poplawsky, L.Q. Ke, W. Tang, I.E. Anderson, M.J. Kramer, On spinodal decomposition in alnico - A transmission electron microscopy and atom probe tomography study, Acta Mater. 153 (2018) 15–22.

[20] H. Kaneko, M. Homma, K. Nakamura, Phase diagram of Fe-Cr-Co permanent magnet system, IEEE Trans. Magn. 13 (1977) 1325–1327.

[21] T. Minowa, M. Okada, M. Homma, Further studies of the miscibility gap in an Fe-Cr-Co permanent magnet system, IEEE Trans. Magn. 16 (1980) 529–533.

[22] V.V. Serikov, N.M. Kleinerman, A.V. Vershinin, E.V. Beloserov, N.V. Mushnikov, G. V. Ivanova, N.N. Shchegoleva, M.A. Uimin, Effect of alloying elements on the structure peculiarities and mechanical properties of high-strength magnetic Fe-Cr-Co based alloys, Solid State Phenom. 168–169 (2011) 388–391.

[23] E.V. Belozerov, N.V. Mushnikov, G.V. Ivanova, N.N. Shchegoleva, V.V. Serikov, N. M. Kleinerman, A.V. Vershinin, M.A. Uimin, High-strength magnetically hard Fe-Cr-Co-based alloys with reduced content of chromium and cobalt, Phys. Met. Metallogr. 113 (2012) 319–325.

[24] L.X. Lv, L. Zhen, C.Y. Xu, X.Y. Sun, Phase field simulation of microstructure evolution in Fe-Cr-Co alloy during thermal magnetic treatment and step aging, J. Magn. Magn. Mater. 322 (2010) 987–995.

[25] R.A. Rastabi, A. Ghasemi, M. Tavoosi, T. Sodaee, Magnetic characterization of nanocrystalline $Fe_{80-x}Cr_xCo_{20}$ ($15 \le x \le 35$) alloys during milling and subsequent annealing, J. Magn. Magn. Mater. 416 (2016) 174–180.

[26] M. Homma, E. Horikoshi, T. Minowa, M. Okada, High-energy Fe-Cr-Co permanent magnets with (BH)max ≃8-10 MG Oe, Appl. Phys. Lett. 37 (1980) 92–93.

[27] Y. Yan, H.R. Shao, D.X. Li, W.G. Lin, G.D. Li, Study of magnetic properties and Mössbauer effect of Fe-Cr-Co permanent magnetic alloys, J. Appl. Phys. 53 (1982) 2377–2379.

[28] K.S. Salimgareev, V.V. Stolyarov, A.V. Korznikov, Effect of the hardening temperature on the structure and properties of magnetically hard Fe-Cr-Co alloy, Met. Sci. Heat Treat. 33 (1991) 634–638.

[29] S. Mahajan, E.M. Gyorgy, R.C. Sherwood, S. Jin, S. Nakahara, D. Brasen, M. Eibschutz, Origin of coercivity in a Cr-Co-Fe alloy (chromindur), Appl. Phys. Lett. 32 (1978) 688–690.

[30] H. Kaneko, M. Homma, T. Fukunaga, M. Okada, Fe-Cr-Co permanent magnent alloys containing Nd and Al, IEEE Trans. Magn. 11 (1975) 1440–1442.

[31] M. Okada, R. Togashi, S. Sugimoto, M. Homma, Radially induced magnetic anisotropy in Fe-Cr-Co permanent magnets, J. Appl. Phys. 64 (1988) 5732–5734.

[32] S. Jin, N.V. Gayle, Low-cobalt Cr-Co-Fe magnet alloys obtained by slow cooling under magnetic field, IEEE Trans. Magn. 16 (1980) 526–529.

[33] X.Y. Sun, C.Y. Xu, L. Zhen, L.X. Lv, L. Yang, Evolution of modulated structure in Fe-Cr-Co alloy during isothermal ageing with different external magnetic field conditions, J. Magn. Magn. Mater. 312 (2007) 342–346.

[34] X.Y. Sun, C.Y. Xu, L. Zhen, L.X. Lu, L.C. Qin, Spinodal decomposition in Fe-25Cr-12Co-1Si alloy under a 100 kOe magnetic field, J. Magn. Magn. Mater. 306 (2006) 69–72.

[35] O.A. Ushakova, E.H. Dinislamova, M.V. Gorshenkov, D.G. Zhukov, Structure and magnetic properties of Fe-Cr-Co nanocrystalline alloys for permanent magnets, J. Alloys Compd. 586 (2014) S291–S293.

[36] T.S. Chin, T.H. Chen, C.Y. Chen, Magnetic properties and microstructures of Fe-Cr-10 wt% Co-M (M= Si/Ti/Ni/Mo/Ge/Ta) permanent magnet alloys, J. Magn. Magn. Mater. 50 (1985) 214–222.

[37] Z. Ahmad, A.U. Haq, S.W. Husain, T. Abbas, Magnetic properties of isotropic Fe-28Cr-15Co-3.5Mo permanent magnets with additives, Phys. B Condens. Matter. 321 (2002) 54–59.

[38] S. Tao, Z. Ahmad, P.Y. Zhang, X.M. Zheng, F. Wang, X.H. Xu, Enhancement of magnetic and microstructural properties in Fe-Cr-Co-Mo-V-Zr-Y permanent magnetic alloy, J. Magn. Magn. Mater. 484 (2019) 88–94.

[39] Z. Ahmad, A.U. Haq, M. Yan, Z. Iqbal, Evolution of phase, texture, microstructure and magnetic properties of Fe-Cr-Co-Mo-Ti permanent magnets, J. Magn. Magn. Mater. 324 (2012) 2355–2359.

[40] M.J. Hÿtch, E. Snoeck, R. Kilaas, Quantitative measurement of displacement and strain fields from HREM micrographs, Ultramicroscopy 74 (1998) 131–146.

[41] P.E. Blöchl, Projector augmented-wave method, Phys. Rev. B. 50 (1994) 17953–17979.

[42] S.L. Dudarev, G.A. Botton, S.Y. Savrasov, C.J. Humphreys, A.P. Sutton, Electron-energy-loss spectra and the structural stability of nickel oxide: an LSDA+U study, Phys. Rev. B. 57 (1998) 1505–1509.

[43] H.J. Monkhorst, J.D. Pack, Special points for Brillonin-zone integrations, Phys. Rev. B. 13 (1976) 5188–5192.

[44] X.H. Han, S.J. Bu, X. Wu, J.B. Sun, Y. Zhang, C.X. Cui, Effects of multi-stage aging on the microstructure, domain structure and magnetic properties of Fe-24Cr-12Co-1.5Si ribbon magnets, J. Alloys Compd. 694 (2017).

[45] Z.L. Xiang, L. Zhang, B.L. An, J. Lu, R.M. Niu, Y. Xin, M. Mardani, T. Siegrist, R. E. Goddard, T.N. Man, T. Wang, E. Wang, K. Han, Effect of evolution of spinodal decomposition on microstructure and properties in multi-step aged FeCrCo alloy, Mater. Charact. 199 (2023) 112764.

[46] Z.L. Xiang, L. Zhang, Y. Xin, B.L. An, R.M. Niu, M. Mardani, T. Siegrist, J. Lu, R. E. Goddard, T.N. Man, E.G. Wang, K. Han, Ultrafine microstructure and hardness in Fe-Cr-Co alloy induced by spinodal decomposition under magnetic field, Mater. Des. 199 (2021) 109383.

[47] Z. Rao, B. Dutta, F. Körmann, W. Lu, X. Zhou, C. Liu, A.K. da Silva, U. Wiedwald, M. Spasova, M. Farle, D. Ponge, B. Gault, J. Neugebauer, D. Raabe, Z. Li, Beyond Solid solution high-entropy alloys: tailoring magnetic properties via spinodal decomposition, Adv. Funct. Mater. 31 (2021).

[48] T.T. Zuo, M.C. Gao, L.Z. Ouyang, X. Yang, Y.Q. Cheng, R. Feng, S.Y. Chen, P. K. Liaw, J.A. Hawk, Y. Zhang, Tailoring magnetic behavior of $CoFeMnNi_X$ (X = Al, Cr, Ga, and Sn) high entropy alloys by metal doping, Acta Mater 130 (2017) 10–18.

[49] C. Jung, K. Kang, A. Marshal, K.G. Pradeep, J.B. Seol, H.M. Lee, P.P. Choi, Effects of phase composition and elemental partitioning on soft magnetic properties of AlFeCoCrMn high entropy alloys, Acta Mater 171 (2019) 31–39.

[50] B.Z. Cui, K. Han, Y. Zhang, J.P. Liu, H. Garmestani, S. Liu, A. Crystallization, crystallization, morphology and magnetic properties of melt-spun $(Nd, Pr, Dy)_2(Fe, Co, Mo)_{14}B$/α–Fe nanocomposites, Ieee Trans. Magn. 40 (2004) 2867–2870.

[51] B.Z. Cui, K. Han, H. Garmestani, J.H. Su, H.J. Schneider-Muntau, J.P. Liu, Enhancement of exchange coupling and hard magnetic properties in nanocomposites by magnetic annealing, Acta Mater. 53 (2005) 4155–4161.

[52] K.Z. Ren, X. Tan, H. Li, H. Xu, K. Han, The effects of the addition of Dy, Nb, and Ga on microstructure and magnetic properties of $Nd_2Fe_{14}B$/α-Fe nanocomposite permanent magnetic alloys, Microsc. Microanal. 23 (2017) 425–430.

[53] L. Zhou, M.K. Miller, P. Lu, L. Ke, R. Skomski, H. Dillon, Q. Xing, A. Palasyuk, M. R. McCartney, D.J. Smith, S. Constantinides, R.W. McCallum, I.E. Anderson, V. Antropov, M.J. Kramer, Architecture and magnetism of alnico, Acta Mater. 74 (2014) 224–233.

[54] S. Drapal, The origin of anisotropy in Fe-Cr-Co alloys, Czech, J. Phys. B. 37 (1987) 1174–1182.

[55] X.M. Liu, X. Zhao, X. Ma, N.H. Wu, Q.Q. Xin, T.X. Wang, Effect of strain on electronic and magnetic properties of n-type Cr-doped WSe_2 monolayer, Phys. E. Nanostructures. 87 (2017) 6–9.

[56] Z.X. Zhao, X.H. Duan, X.T. Fang, X.C. Wang, W. Mi, Prediction of electronic structure and magnetic anisotropy of two-dimensional MSi_2N_4 (M = 3d transition-metal) monolayers, Appl. Surf. Sci. 611 (2023) 155693.

[57] Y.M. Liu, F. Wang, D.C. Kong, B. Hu, C.X. Xia, J.X. Su, Effect of strain on electronic and magnetic properties of Fe-doped monolayer SnS2, Phys. Lett. Sect. A Gen. At. Solid State Phys. 381 (2017) 1732–1737.

[58] J. Lyubina, I. Opahle, K.H. Müller, O. Gutfleisch, M. Richter, M. Wolf, L. Schultz, Magnetocrystalline anisotropy in $L1_0$ FePt and exchange coupling in FePt/Fe_3Pt nanocomposites, J. Phys. Condens. Matter. 17 (2005) 4157–4170.

[59] L. Zhang, K. Han, X.R. Zhang, E.G. Wang, J. Lu, R. Goddard, Effect of a high magnetic field on hard magnetic multilayered Fe-Pt alloys, J. Magn. Magn. Mater. 490 (2019) 165533.
[60] Y.X. Jia, Y.Y. Wu, S. Zhao, S.L. Zuo, K.P. Skokov, O. Gutfleisch, C.B. Jiang, H.B. Xu, L_{10} rare-earth-free permanent magnets: the effects of twinning versus dislocations in Mn-Al magnets, Phys. Rev. Mater. 4 (2020) 94402.
[61] M. Yi, H.B. Zhang, O. Gutfleisch, B.X. Xu, Multiscale examination of strain effects in Nd-Fe-B permanent magnets, Phys. Rev. Appl. 8 (2017) 1–11.
[62] H. Zheng, J. Wang, S.E. Lofland, Z. Ma, L. Mohaddes-Ardabili, T. Zhao, L. Salamanca-Riba, S.R. Shinde, S.B. Ogale, F. Bai, D. Viehland, Y. Jia, D.G. Schlom, M. Wuttig, A. Roytburd, R. Ramesh, Multiferroic $BaTiO_3$-$CoFe_2O_4$ nanostructures, Science 303 (2004) 661–663.
[63] Y.F. Xu, Y.Q. Ma, S.T. Xu, F.L. Zan, G.H. Zheng, Z.X. Dai, Obtainment of exchange coupling coefficient of $Ni_{0.6}Zn_{0.4}Fe_2O_4/SrFe_{12}O_{19}$ composites, Mater. Lett. 131 (2014) 203–205.
[64] B.Z. Cui, C.T. Yu, K. Han, J.P. Liu, H. Garmestani, M.J. Pechan, H.J. Schneider-Muntau, Magnetization reversal and nanostructure refinement in magnetically annealed $Nd_2Fe_{14}B$/α-Fe -type nanocomposites, J. Appl. Phys. 97 (2005) 33–36.
[65] W.B. Cui, H. Sepehri-Amin, Y.K. Takahashi, K. Hono, Hard magnetic properties of spacer-layer-tuned NdFeB/Ta/Fe nanocomposite films, Acta Mater 84 (2015) 405–412.
[66] T. Kakeshita, T. Fukuda, Effects of magnetic field on martensitic transformations, J. Phys. Conf. Ser. 165 (2009) 21–39.
[67] T. Kawagoe, Y. Suzuki, M. Nývlt, J. Franta, N. Hosoito, Magnetic domain structure and exchange coupling in epitaxial Fe/FeRh(001) and NiFe/FeRh(001) bilayers, Surf. Sci. 493 (2001) 721–730.
[68] X.H. Tan, S.F. Chan, K. Han, H. Xu, Combined effects of magnetic interaction and domain wall pinning on the coercivity in a bulk $Nd_{60}Fe_{30}Al_{10}$ ferromagnet, Sci. Rep. 4 (2014) 1–5.
[69] J. Thielsch, H. Stopfel, U. Wolff, V. Neu, T.G. Woodcock, K. Güth, L. Schultz, O. Gutfleisch, In situ magnetic force microscope studies of magnetization reversal of interaction domains in hot deformed Nd-Fe-B magnets, J. Appl. Phys. 111 (2012) 103901.
[70] K. Zhang, Z. Fu, Effects of annealing treatment on properties of CoCrFeNiTiAl*x* multi-component alloys, Intermetallics 28 (2012) 34–39.
[71] S. Jin, S. Mahajan, D. Brasen, Mechanical properties of Fe-Cr-Co ductile permanent magnet alloys, Metall. Mater. Trans. A. 11 (1980) 69–76.
[72] T.S. Chin, T.S. Wu, C.Y. Chang, T.K. Hsu, Y.H. Chang, Electron microscopy and magnetic properties of Fe-Cr-Co-Si permanent magnet alloys manufactured by rolling-ageing technique, J. Mater. Sci. 18 (1983) 1681–1688.
[73] H. Kaneko, M. Homma, K. Nakamura, M. Miura, Fe-Cr-Co permanent magnet alloys containing silicon, IEEE Trans. Magn. 8 (1972) 347–348.
[74] R.K. Mishra, P. Kumari, A.K. Gupta, R.R. Shahi, Design and development of $Co_{35}Cr_5Fe_{20-x}Ni_{20+x}Ti_{20}$ high entropy alloy with excellent magnetic softness, J. Alloys Compd. 889 (2022) 161773.
[75] T. Borkar, V. Chaudhary, B. Gwalani, D. Choudhuri, C.V. Mikler, V. Soni, T. Alam, R.V. Ramanujan, R. Banerjee, A combinatorial approach for assessing the magnetic properties of high entropy alloys: role of Cr in $AlCoxCr_{1-x}FeNi$, Adv. Eng. Mater. 19 (2017) 1–13.
[76] K.B. Zhang, Z.Y. Fu, J.Y. Zhang, J. Shi, W.M. Wang, H. Wang, Y.C. Wang, Q. J. Zhang, Annealing on the structure and properties evolution of the CoCrFeNiCuAl high-entropy alloy, J. Alloys Compd. 502 (2010) 295–299.
[77] V. Chaudhary, V. Soni, B. Gwalani, R.V. Ramanujan, R. Banerjee, Influence of non-magnetic Cu on enhancing the low temperature magnetic properties and Curie temperature of FeCoNiCrCu(*x*) high entropy alloys, Scr. Mater. 182 (2020) 99–103.